ROUTING AND ACTION
MEMORANDUM

ROUTING

TO: (1) Life Sciences Division (Gregory, Frederick)

Report is available for review

(2) Proposal Files Proposal No.: 71227-LS

DESCRIPTION OF MATERIAL

CONTRACT OR GRANT NUMBER: W911NF-18-1-0323

INSTITUTION: University of Wisconsin - Milwaukee

PRINCIPAL INVESTIGATOR: Ramin Pashaie

TYPE REPORT: Interim Progress Report

DATE RECEIVED: 10/3/19 3:21PM

PERIOD COVERED: 01-Aug-2018 through 31-July-2019

TITLE:

ACTION TAKEN BY DIVISION

(x) Report has been reviewed for technical sufficiency and IS [x] IS NOT [ ] satisfactory.

(x) Material has been given an OPSEC review and it has been determined to be non sensitive and, except for manuscripts and progress reports, suitable for public release.

Approved by SSL\FREDERICK.GREGORY on 3/2/20 8:48AM

ARO FORM 36-E

REPORT DOCUMENTATION PAGE

Form Approved OMB NO. 0704-0188

The public reporting burden for this collection of information is estimated to average 1 hour per response, including the time for reviewing instructions, searching existing data sources, gathering and maintaining the data needed, and completing and reviewing the collection of information. Send comments regarding this burden estimate or any other aspect of this collection of information, including suggesstions for reducing this burden, to Washington Headquarters Services, Directorate for Information Operations and Reports, 1215 Jefferson Davis Highway, Suite 1204, Arlington VA, 22202-4302. Respondents should be aware that notwithstanding any other provision of law, no person shall be subject to any oenalty for failing to comply with a collection of information if it does not display a currently valid OMB control number.
PLEASE DO NOT RETURN YOUR FORM TO THE ABOVE ADDRESS.

1. REPORT DATE (DD-MM-YYYY)	2. REPORT TYPE	3. DATES COVERED (From - To)
03-10-2019	Interim Progress Report	1-Aug-2018 - 31-Jul-2019

4. TITLE AND SUBTITLE
Brain Functional Imaging via Optical Coherence Tomography

5a. CONTRACT NUMBER
W911NF-18-1-0323

5b. GRANT NUMBER

5c. PROGRAM ELEMENT NUMBER
611102

6. AUTHORS

5d. PROJECT NUMBER

5e. TASK NUMBER

5f. WORK UNIT NUMBER

7. PERFORMING ORGANIZATION NAMES AND ADDRESSES
University of Wisconsin - Milwaukee
P.O. Box 340

Milwaukee, WI 53201 -0340

8. PERFORMING ORGANIZATION REPORT NUMBER

9. SPONSORING/MONITORING AGENCY NAME(S) AND ADDRESS (ES)
U.S. Army Research Office
P.O. Box 12211
Research Triangle Park, NC 27709-2211

10. SPONSOR/MONITOR'S ACRONYM(S)
ARO

11. SPONSOR/MONITOR'S REPORT NUMBER(S)
71227-LS

12. DISTRIBUTION AVAILIBILITY STATEMENT
Approved for public release; distribution is unlimited.

13. SUPPLEMENTARY NOTES
The views, opinions and/or findings contained in this report are those of the author(s) and should not contrued as an official Department of the Army position, policy or decision, unless so designated by other documentation.

14. ABSTRACT

15. SUBJECT TERMS

16. SECURITY CLASSIFICATION OF:			17. LIMITATION OF ABSTRACT	15. NUMBER OF PAGES	19a. NAME OF RESPONSIBLE PERSON
a. REPORT	b. ABSTRACT	c. THIS PAGE			Ramin Pashaie
UU	UU	UU	UU		19b. TELEPHONE NUMBER 414-229-2273

RPPR Interim Progress Report
as of 02-Mar-2020

Agency Code:

Proposal Number: 71227LS **Agreement Number: W911NF-18-1-0323**
INVESTIGATOR(S):

Name: Ramin Pashaie
Email: pashaie@uwm.edu
Phone Number: 4142292273
Principal: Y

Organization: **University of Wisconsin - Milwaukee**
Address: P.O. Box 340, Milwaukee, WI 532010340
Country: USA
DUNS Number: 627906399 EIN: 391805963

Report Date: 31-Aug-2019 Date Received: 03-Oct-2019
Interim Progress Report for Period Beginning 01-Aug-2018 and Ending 31-Jul-2019
Title: Brain Functional Imaging via Optical Coherence Tomography
Begin Performance Period: 01-Aug-2018 **End Performance Period:** 29-Feb-2020
Report Term: 1-Annual

Submitted By: Ramin Pashaie Email: pashaie@uwm.edu
Phone: (414) 229-2273

Distribution Statement: 1-Approved for public release; distribution is unlimited.

STEM Degrees: **STEM Participants:**

Major Goals: The main goal of the project is to study the dynamics of the coupling between the vascular network and neural circuits in the brain. We intend to learn details of this dynamics and use this coupling to map neural activity by recording from vascular network.
Blood flow in the brain is well regulated via cell signaling pathways. Since neurons are among the most active cells in the brain, stimulation of neuron almost always leads to some level of increase in the regional blood flow. Nonetheless, since the network of vessels is a complex system, blood flow increase in one area can temporarily lead to reduction of flow in another region. We proposed to develop new brain interface platforms and conduct experiments to study subtle features of this complex dynamics and use it to map neural activity.
In the first phase of the project, we built our optoelectronic brain interface platform in which advanced technologies including ECoG recording, Optogenetic stimulation, Fluorescence microscopy, and Spectral domain optical coherence tomography where combined in one experimental platform. The system allows us to selectively stimulate neuron via optogenetics, record neural activity via ECoG electrophysiology or fluorescence imaging, and measure the vascular response via coherence tomography. In phase two that we finished last year, we used all the collected data from our experiments, to study details of neuro vascular coupling and develop the mathematical models. In the next phase, we intend to use our setup and the developed model to see how accurately we can predict neural activity by only looking at the dynamics of the vessels and capillaries.

Accomplishments: Phase 1: development of the experimental setup in which ECoG recording, Optogenetic stimulation, Fluorescence Microscopy, and Optical coherence tomography were integrated in one platform.

Paper was submitted and published at this point. Journal of Neural Engineering

Phase 2: We designed more advanced experiments and collected large datasets. We used the data to generate mathematical models that shows details of the coupling between neural circuits and the vascular network. We transform our findings to a mathematical model that could predict the behavior of the vascular network when responding to neural activation in open-loop and closed-loop experiments.

Paper was submitted. We have heard from the reviewers and they have asked for revisions. We are currently preparing our response and the deadline for submission of the revised manuscript is Oct. 29th, 2019. The review in general is positive. We believe by providing reasonable responses to the questions and applying some modifications to the text, the paper will be accepted for publication. Journal of Neural Engineering

RPPR Interim Progress Report
as of 02-Mar-2020

Training Opportunities: When we started the project, I had 2 PhD students on board working actively on the project. One PhD student (Dr. Farid Atry) finished his program and graduated. The second PhD student is still working with me on the project. I also recruited a new PhD student that is receiving support from this funding and I am training the new student who will take over when my current active PhD student graduate in about one year from now.

I also provided research opportunity for two local undergraduate student who are working in the lab and together they are developing a new experimental setup which will allow us to image oxygen consumption in the brain tissue during optogenetic stimulation. This is very important factor since metabolic signaling is also involved in the process of neuro-vascular coupling and with the help of these two students we are moving in the direction of adding this parallel capability to our current experimental setup. The work in a combination of hardware and software development for data acquisition and data analysis. I believe this is a great opportunity for these two undergraduate students. Fortunately, we were successful in getting some funding from our university to support these two students during their work on the project. The money from Army Research Office is used mainly to support PhD students and the purchase of equipment for their project.

Results Dissemination: Nothing to Report

Plans Next Period: With the setup ready to generate data and with the model developed, we can move to next phase of the project in which we will test our capability in terms of estimating neural activity (level and spatial distribution) by only recording from vascular network. This is the next logical phase for the project. We will also add the capability to better track metabolic signals and their timings in the next phase.

Honors and Awards: Nothing to Report

Protocol Activity Status:

Technology Transfer: Nothing to Report

PARTICIPANTS:

Participant Type: Graduate Student (research assistant)
Participant: Rex Chen
Person Months Worked: 6.00 **Funding Support:**
Project Contribution:
International Collaboration:
International Travel:
National Academy Member: N
Other Collaborators:

Participant Type: Graduate Student (research assistant)
Participant: Rex Chen
Person Months Worked: 6.00 **Funding Support:**
Project Contribution:
International Collaboration:
International Travel:
National Academy Member: N
Other Collaborators:

Participant Type: Graduate Student (research assistant)
Participant: Rex Chen
Person Months Worked: 6.00 **Funding Support:**
Project Contribution:
International Collaboration:
International Travel:
National Academy Member: N
Other Collaborators:

RPPR Interim Progress Report

as of 02-Mar-2020

Participant Type: Graduate Student (research assistant)
Participant: Rex Chen
Person Months Worked: 6.00 **Funding Support:**
Project Contribution:
International Collaboration:
International Travel:
National Academy Member: N
Other Collaborators:

System Engineering Analysis of Optogenetically Evoked Local Field Potential and Cerebral Blood Flow Response

Rex Chin-Hao Chen, Farid Atry, Aaron J. Suminski, Thomas Richner, Sarah Brodnick, Daniel T. Patel, Jane Pisaniello, Jared Ness, Justin Williams, Ramin Pashaie†,

***Abstract*—A combination of advanced technologies were used to study the coupling between neural circuits and the vascular network in the cortex of small rodents. Optogenetics was used to selectively stimulate predefined population of neurons while the induced local field potentials and hemodynamic responses were being collected by electrocorticography arrays and spectral-domain optical coherence tomography, respectively. System identification methods were adopted to analyze the relation between the input (induced neural activity) and observable outputs (electrophysiology and blood flow response) with the goal of producing a mathematical model that captures essential elements of these dynamics. The resulting model, once trained on experimental data, successfully regenerated subtle spatiotemporal features of the evoked local field potentials and cerebral blood flow responses following the onset of optogenetic neural stimulation. The long term goal of this research is to open a new line for computational analysis of neurovascular coupling in the brain, particularly in pathologies where the normal process of blood flow regulation is disrupted, including ischemic stroke, hypertension, and Alzheimer's disease.**

***Index Terms*—optogenetics, optical coherence tomography, cerebral blood flow, dynamic causal modeling, and neurovascular coupling.**

I. Introduction

THE impressive performance of the brain is the result of the dynamics of two interconnected networks. The first network is the network of coupled neurons in which each cell functions as a nonlinear complex processing element. The topography of this network is shaped by development learning and plasticity. Data processing and other high level brain functions, including perception, cognition, consciousness, and intelligent acts, are outcomes of the dynamics of these circuits. The second network is the vascular system which is spatially distributed throughout the three dimensional structure of the brain. The main task of this network, which is developed through the adaptive process of angiogenesis, is to regulate the delivery of vital metabolic and respiratory substances to nerve cells and removal of metabolic byproducts (MBP). Dynamics of these two networks are intimately tied to the point that hemodynamic responses are used in some advanced neuro-imaging modalities, e.g., functional magnetic resonance imaging (fMRI), to indirectly map the distribution of neural activity in the brain.

Understanding mechanisms underlying neurovascular coupling (NVC) is scientifically important since their study provides insight into the brain's information processing pathways and pathophysiology of disorders in which the NVC is perturbed including ischemic stroke, hypertension, vascular oxidative stress, and Alzheimer's.

Study of NVC can be done at the cellular or molecular level where the research is focused on understanding the role of each cell type involved in the process or molecules that mediate the coupling between neurons and the vascular network. This paper specifically concentrates on the study of NVC from system engineering point of view. In this approach, we assume that NVC is a system of inputs (patterns of neuro-stimulation) and outputs (vessel dilation/contraction or changes in blood velocity profiles). By designing parametric stimulation inputs and observing the corresponding outputs, we probed the dynamics of this system. The goal of this research is to form a mathematical framework that formulates how the vascular network responds to neural stimulation.

It is generally accepted that multiple cellular and metabolic signaling mechanisms contribute to form the response of the vascular network to the onset of neural activity [1], [2]. When we stimulate neurons, the response of the vascular network or the blood flow fluctuations, can be decomposed to two distinct terms which contribute to the vascular response with different time-constants. These two contributing elements are known as the *acute* and *delayed* responses. Recently, researchers used a combination of advanced technologies to study NVC and their experimental findings were summarized as the *unified theory of NVC* [1]. This theory provides plausible justification for the appearance of acute and delayed responses. According to this theory, the acute response, is mediated by a fast electrical signaling mechanism [3], [4]. Longden et al. explained that the endothelial cells, which form the structure of capillaries, have a specific type of K^+-channel known as the inward-rectifier K^+-channel, Figure 1. When neurons fire, astrocytes regulate an increase in the extracellular K^+ concentration, $[K^+]$, which leads to the opening of inward-rectifier K^+-channels and hyperpolarization of endothelium cells. This hyperpolarizing

† Correspondence should be directed to: Ramin Pashaie, e-mail: pashaie@uwm.edu

Rex Chen, Daniel Patel, and Ramin Pashaie are with the Electrical and Computer Engineering Department, University of Wisconsin-Milwaukee, 3200 N Cramer St., Milwaukee, WI, USA.

Thomas Rcihner is with the Biomedical Engineeirng Department, University of Minnesota, Minneapolis, MN, USA.

Farid Atry, Sarah Brodnick, Aaron J. Suminski, Jane Pisaniello, Jared Ness, and Justin Williams are with the Department of Biomedical Engineering, University of Wisconsin-Madison, Madison, WI, USA.

Manuscript received —-;

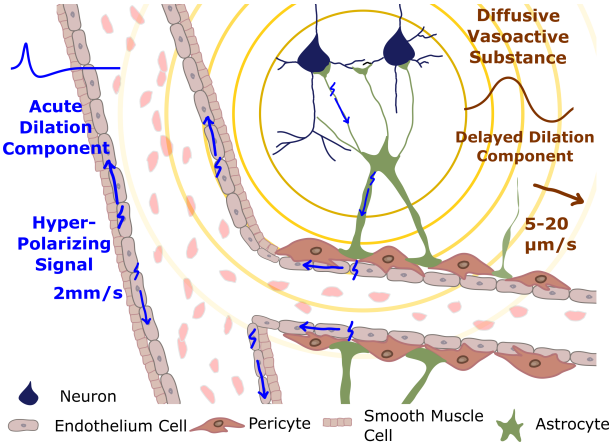


Fig. 1. Two distinct vasodilation components, the acute and delayed responses, can both evoke cerebral blood flow. Acute dilation component: When neurons fire, astrocytes regulate an increase in the extracellular $[K^+]$. The increase in $[K^+]$ leads to the opening of inward-rectifier K^+-channels in endothelial cells which initiates a hyperpolarizing signal that propagates toward the upstream arterioles/arteries and deactivates voltage-dependent Ca^{2+}-channels of smooth muscle cells and vessels (artery and arterioles) dilate. The acute component serve as a feed-forward system that continuously monitors the activity of neurons through webs of sensors (capillaries) and quickly address the metabolic demands of neurons by sending electrical signals to upstream vessels. Acute dilation component evokes blood flow that is highly consistent with the neural activity and is employed in fMRI technology for brain mapping. Delayed dilation component: As neurons fire, MBPs are released into the extracellular space which travel through molecular diffusion to reach pericyte and smooth muscle cells and cause vasodilation in capillaries, arterioles, and arteries. As vessels dilate, the flow removes MBPs and the vasodilation stops.

signal propagates along endothelium cells toward the upstream arterioles/arteries and deactivates voltage-dependent Ca^{2+}-channels of smooth muscle cells. Consequently, these vessels dilate and blood flow increases within a few tens of millisecond. From this point of view, capillaries function as a sensor-network and help the tissue rapidly respond to the metabolic demand of cells. Chen et al. estimated that the propagation velocity of the associated vasodilation signal is around $2mm/s$ [3]. Due to this short response-time, the acute mechanism is considered by many researchers as the main origin of blood oxygenation level dependent (BOLD) signal that conventional fMRI scanners record.

It is hypothesized that the delayed response is the output of a feedback system which functions to maintain the local concentration of MBPs within an acceptable range. The most common MBPs are NO and CO_2 which are vasodilators. The onset of neural activity causes some increase in the local concentration of MBPs and as a result, vessels in the region dilate and blood flow raises locally. The increased flow of blood reduces the concentration of MBPs and vessels constrict. The production and dissipation of MBPs are time-consuming processes. Cai et al. observed slowly propagating vasomotion spreading at the speed of about $5\mu m/s$ to $20\mu m/s$ [5]. This vasomotion occurs in both arterioles and capillaries where pericytes are the main regulators of the vessel dilation or constriction.

For the study of NVC, we need technologies to stimulate neurons and simultaneously monitor induced neural activity and corresponding fluctuations in the regional blood flow. In this work, we used optogenetics to reversibly stimulate a selected population of neurons [6], [7], [8], [9], [10]. To record hemodynamic signals, we developed our spectral-domain optical coherence tomography (SD-OCT) scanner which is a suitable technology to image most vessels and capillaries in the cortical tissue of small rodents even through the bone (thinned skull) [11], [12], [13], [14]. By employing OCT angiography (OCA) and Doppler Coherence Tomography (DCT), we built a system capable of measuring dilation/contraction or changes in blood velocity profile in every cortical vessel within the field of view.

Electrophysiology is one of the most reliable technique nowadays to monitor neural activity in the brain. Here, we used electrode arrays placed over the cortical surface, electrocorticography (ECoG) arrays, to record local field potentials (LFP). In recent years, we microfabricated and tested semi- [17] or fully transparent ECoG electrode arrays including our carbon-layered electrode array ECoG, a.k.a, Clear-ECoG [15], [16]. We epidurally implanted transparent ECoGs onto the brain and under a cranial window. This configuration provided optical access to the brain tissue for stimulation and imaging as we record LFPs.

We formed a mathematical model that captures the main features of the process including optogenetic stimulation and generation of LFPs and hemodynamic responses. Next, we conducted experiments on this hybrid brain interface platform and acquired necessary data to optimize parameters of the model and validate its performance. Architecture of the model, design of the experimental setup, procedures of data acquisition and processing, and adopted model development and verification algorithms are discussed in this article.

II. Architecture of the Model

The architecture of the model we intend to develop in this paper is displayed in Figure 2. The process starts at the optogenetic stimulation of neurons. In this study, we used Thy1-Chr2(H134R) transgenic optogenetic mice for all experiments (Jax stock 012350). The main light-sensitive cell population in these experiments was excitatory pyramidal neurons of the somatosensory cortex which express Channelrhodopsin-2 (ChR2) light-gated cation channels. Light exposure opens ChR2 channels and generates photocurrent in these cells, Figure 2a. Excitatory neurons in the cortex are synaptically coupled to the inhibitory neural population. Optically stimulated pyramidal cells activate inhibitory neurons which provide a negative feedback mechanism that ultimately adjusts the overall level of cellular activity in the region, Figure 2b. The generated photocurrent and the corresponding induced activity in excitatory and inhibitory cells contribute to LFP signals that were recorded by the ECoG array during experiments. In this model, activated neurons trigger the reaction in the vascular network through two separate pathways which yielding the acute and delayed responses, Figure 2c. The hemodynamic response is another output or observable of the model that was recorded by the coherence tomography platform during our experiments.

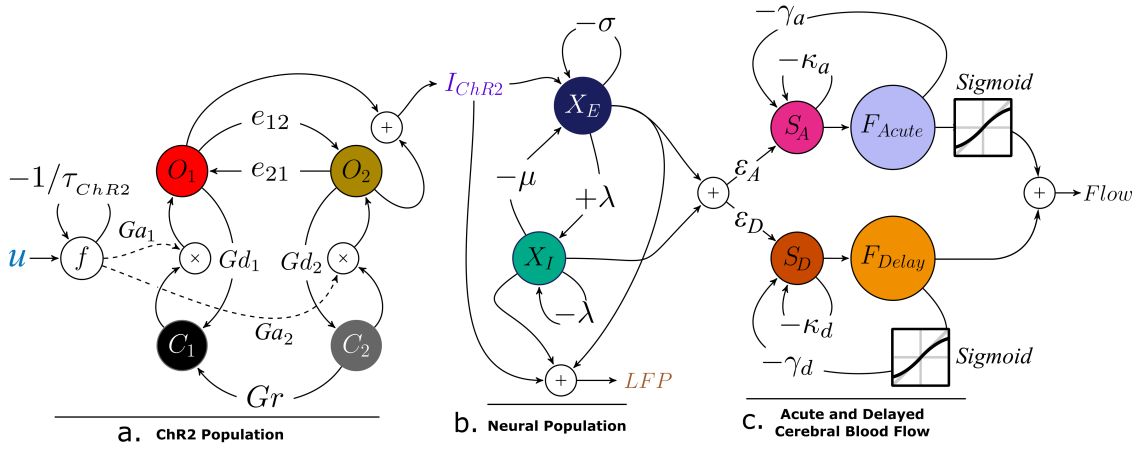


Fig. 2. Schematic of the model. (a) Optogenetic stimulation: each ChR2 channel has four states, two open (O_1 and O_2) and two close states (C_1 and C_2). Open states permit the flux of cations and form a transmembrane photocurrent, (b) the transmembrane photocurrent leads to the rise of membrane potential in excitatory neurons. Activated excitatory neurons stimulate inhibitory cells via synaptic couplings. The LFP signal that is recorded by electrodes is proportional to the superposition of the activity in both cell populations and the induced photocurrent, (c) the blood flow response is modeled by two separate pathways to incorporate the effect of acute and delayed responses where each pathways has two state-space variables as discussed in the paper. To better capture the observed nonlinear behavior, we have added two sigmoidal functions to the model, one in the feedback path of the delayed response, and another at the output stage of the acute response.

A. Optical Stimulation Model

To mathematically formulate the response of ChR2 channels to light exposure, we adopted the four-state model which has seven identifiable parameters [40]. This model offers a good balance between parameter identifiability and accuracy, Figure 2a. Here, every channel is in one of the four possible states at each point in time. These states are: (1) open state with high conductance, O_1, (2) open state with low conductance, O_2, (3) closed state with zero conductance, C_2, which is the second least energetic state, and (4) closed ground-state, C_1, which is the state with the lowest energy. In our notation, $[O_{1,2}]$ and $[C_{1,2}]$ represents the relative number of channels in each state; therefore, after normalization, we have: $[O_1]+[O_2]+[C_1]+[C_2]=1.0$. Under no exposure, all channels are in the ground-state, C_1. When exposed to light, some channels absorb photons and enter the O_1 state. The O_1 state has a short lifetime; therefore, each channel in this state soon after transits to O_2 state first and then to C_2. Channels in the C_2 state can get re-excited back to the O_2 state or further decay into C_1. While the signal flow chart in Figure 3a shows many different transition possibilities, the most common transition path is the ring-like dynamics which follows the trajectory: $C_1 \rightarrow O_1 \rightarrow O_2 \rightarrow C_2 \rightarrow C_1$. The combined conductance of the O_1 and O_2 states determines the magnitude of the photocurrent, I_{ChR2}.

The autonomous model that captures interstate transitions was formulated with a set of four differential equations. Absorption of light by the light-sensitive atomic bond of the retinal molecule embedded in the ChR2 structure leads to a conformational change which happens in microseconds. This conformational change puts mechanical pressure on the ChR2 molecule which opens the channel. Opening of the channel is relatively a more time-consuming process and takes up to a few milliseconds, typically $\sim 1.3ms$ [20] for the regular ChR2, and $\sim 1.92ms$ [21] for the $H134R$ point-mutant variation of ChR2. The ChR2 channel opening can be modeled by the following first order differential equation:

$$\dot{f(t)} = \frac{1}{\tau_{ChR2}}\left[-f(t)+u(t)\right]. \tag{1}$$

In this equation, $f(t)$ represents the number of photons absorbed by the retinal in a ChR2 molecule per unit of time and $\tau_{ChR2}(sec)$ is the time-constant of the process. $u(t)$ is proportional to the number of photons that arrive at the cross-section of retinal molecules per unit of time:

$$u(t) \propto \frac{\sigma_{ret}\cdot\phi}{E\cdot W_{loss}}, \tag{2}$$

where σ_{ret} is the retinal molecule cross-section, (e.q., $1.210^{-20}m^2$), ϕ is the irradiance, $W_{loss} \geq 1.0$ is a measure of photon loss caused by light absorption or scattering in the medium, and E is the photon energy. When a ChR2 positive neuron is exposed to light, the activation rate which affects the number of channels in C_1 state transiting to O_1 is:

$$G_{a1} = \epsilon_1 \cdot f(t). \tag{3}$$

Here, ϵ_1 is the quantum efficacy coefficient. The inter-state transition process can be modeled by the following set of differential equations:

$$[\dot{O_1}] = G_{a1}[C_1] - (G_{d1}+e_{12})[O_1] + e_{21}[O_2], \tag{4}$$
$$[\dot{O_2}] = G_{a2}[C_2] - (G_{d2}+e_{21})[O_2] + e_{12}[O_1], \tag{5}$$
$$[\dot{C_2}] = G_{d2}[O_2] - (G_{a2}+G_r)[C_2]. \tag{6}$$

Similar to the $C_1 \rightarrow O_1$ transition, the number of channels in C_2 state that enter O_2 can be calculated by:

$$G_{a2} = \epsilon_2 \cdot f(t). \tag{7}$$

A fraction of channels at O_1 state eventually decay into the less energetic conductive O_2 state with the rate-constant e_{12}.

Some channels re-enter the O_1 state from O_2 with the rate-constant e_{21}. Direct degradation from O_1 to C_1 or from O_2 to C_2 also take place with the grounding-rates G_{d1} and G_{d2}, respectively. In these equations, the coefficient G_r represents the grounding-rate of channels transiting from C_2 to C_1. Finally, the photocurrent, which is the result of the exposure, can be calculated from:

$$I_{ChR2} = I_{max}(O_1 + \nu \cdot O_2), \tag{8}$$

where I_{max} is the maximum possible current and $\nu \leq 1.0$ is the conductance-ratio between O_1 and O_2.

We can consider two models to simulate the effect of the generated photocurrent on the activity level of local neural populations. In the single-state neuron model, we assume that the light exposure only affects the activity of excitatory neurons, χ_E, following a first order differential equation with decay constant σ and excitation coefficient c:

$$\dot{\chi_E} = -\sigma \cdot \chi_E + c \cdot I_{ChR2}. \tag{9}$$

On the other hand, in the two-state neuron model, we also take into account that excitatory neurons are synaptically coupled to inhibitory cells. Therefore, activation of excitatory neurons also affects the activity level of inhibitory cells, χ_I, and vice verse.

$$\dot{\chi_E} = -\sigma \cdot \chi_E - \mu \cdot \chi_I + c \cdot I_{ChR2}, \tag{10}$$

$$\dot{\chi_I} = \lambda \cdot \chi_E - \lambda \cdot \chi_I. \tag{11}$$

In this model, increasing the activity of excitatory neurons, χ_E, increases the activity of inhibitory cells, χ_I, with the rate-constant λ, while activated inhibitory cells try to suppress the activity of excitatory population with the rate-constant μ. Consequently, these two cell populations, together, form a dynamics with a negative feedback. Nevertheless, the activity level of both cell populations eventually lessen over time.

Historically, Friston et al. [22] first proposed the single-state neuron model. Later, Marreiros et al. [23] introduced the two-state model to incorporate the effect of inhibitory neurons on the dynamics and the generated feedback loop. The parameter λ was later added to the model by Havlicek et al. [24] to make the model more plausible.

B. Optogenetically Evoked Local Field Potential Model

The LFP is an electric signal which is generated by a population of neurons acting as in-phase current sources [25]. Superposition of these currents generates a field which induces an electric potential on recording electrodes.

Within somatosensory cortex, which is the main target in this research, cell bodies of the ChR2 expressing pyramidal neurons are spatially distributed in the layer V of the cortex with their apical dendrites spreading into layer I, aligned normal to the cortical surface, Figure 3. Blue photons applied to the brain at the surface scatter as they penetrate deeper into the tissue. Therefore, the density of activated ChR2 channels in each pyramidal neuron decreases from dendrites down to the soma [26]. Each open ChR2 channel generates a net influx of cations. This transmembrane photocurrent displaces other intracellular cations and pushes them away to more distal areas. Displacement of ions produces an electric dipole with the negative potential at the extracellular area closer to the surface and positive potential deeper inside the tissue. These dipoles form current-sinks near the surface and current-sources near somas. Because the relative distance between the surface electrode and current-sinks in layer I is less than the distance between the same electrode and current-sources of layer V, in response to each optogenetic stimulation pulse, the surface electrode records a negative potential relative to a reference electrode placed several millimeters away from the site of stimulation. Furthermore, as cations enter excitatory neurons due to blue light illumination and depolarize the cells, voltage-gated ion channels open as well which further contributes to the negative potential recorded at the surface. Generated excitatory post synaptic potentials (EPSPs) stimulate both excitatory and inhibitory neurons in the neighboring areas. Meanwhile, stimulated inhibitory neurons and their inhibitory postsynaptic potentials (IPSPs) contribute to the LFP signal in an opposite way since the activity of these cells create current sources near the surface which raises the recorded LFP. The generated LFP is the weighted superposition of the photocurrent and the activity of both neural populations:

$$LFP = \zeta_{ChR2} \cdot I_{ChR2} + \zeta_E \cdot \chi_E - \zeta_I \cdot \chi_I. \tag{12}$$

Here, the efficacy of each component is incorporated in the model by coefficients ζ_{ChR2}, ζ_E and ζ_I. We validated this model by the data we collected under different stimulation configurations as discussed in the following sections.

C. Optogenetically Evoked Cerebral Blood Flow Model

1) M_0 Single-Path Single-State Model: In this formulation, inputs to the NVC model are the postsynaptic activity of neurons which are χ_E and χ_I. Here, the CBF response is described as an exponential decay function with the self-decay time-constant τ:

$$\dot{F} = \frac{-1}{\tau} \cdot F + \epsilon \cdot [\chi_E + \eta \cdot \chi_I], \tag{13}$$

where η is the efficacy ratio between the excitatory and inhibitory activity, and ϵ parameterizes the influence of neural activity in the region. During optimization, η was allowed to take negative or positive values. The reason is that stimulated inhibitory neurons reduce the activity of both cell populations which causes blood flow reduction. Nonetheless, active inhibitory neurons also produce MBPs that function as vasodilators.

2) M_1 Single-Path Dual-State Model: For the two-state NVC model, we adopted the feedback structure proposed by Friston and colleagues [27], [28], [29]. In this model, state variables are the fluidic resistance r and the vasodilative molecule concentration S. Neural activation acts as an exogenous input to the equation and causes some increase in the local concentration of vasodilative molecules, represented by the state variable S. Elevation in the local concentration of vasodilative chemicals leads to the relaxation of muscular

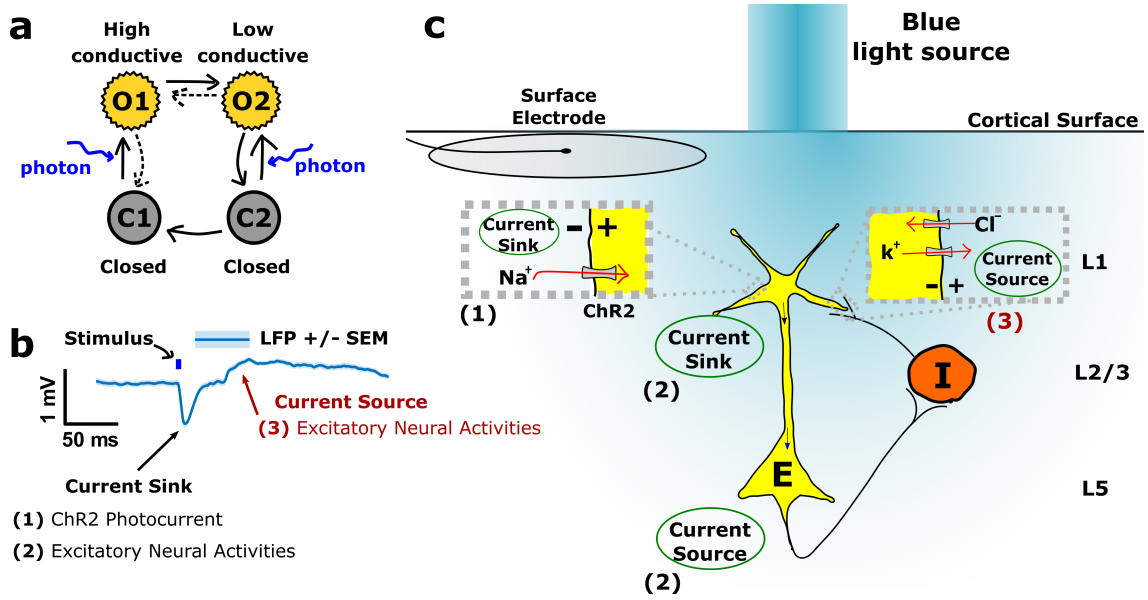


Fig. 3. Biophysics of the optogenetically evoked local field potentials (LFPs). (a) ChR2 channels probabilistically transition between open states and closed states, generating a photocurrent when light is applied. (b) A surface electrode recording of a typical LFP signal evoked by a short-pulse optogenetic stimulation. The signal contains an initial dip that correspond to the stimulation pulse with a fast decaying rate constant. After the pulse terminates, a slow rebound signal appears with an overshoot which eventually decays back to the resting state. (c) The general physical arrangement of excitatory and inhibitory cells in the somatosensory cortex. Pyramidal excitatory neurons (marked by letter E) are commonly aligned axially while their apical dendrites near the surface. Inhibitory neurons (marked by letter I) are located in layer 2/3 and their synapse connects with the apical dendrites of excitatory cells. When light illuminates the tissue from the surface, the photon flux reduces as the light penetrates deeper. As a result, the maximum activation density of ChR2 proteins happens at regions closer to the surface where apical dendrites are located. Open ChR2 channels (1) create a current sink as sodium enters the cells, leaving a net negative charge that draws current from the surrounding, resulting in a negative potential which is recorded by the surface electrode as displayed in panel (b). As the magnitude of the photocurrent increases, excitatory cells (2) fire, further amplifying the signal and creating an electric dipole with a current sink in Layer I and a current source in deeper layers. As excitatory cells fire, they increase the activity of inhibitory cells (3) which results in the opening of chloride and potassium channels. The ionic current of both channels leaves positive charge outside cells which produces current source and forms the rebound signal in the recorded LFP.

mural cells (smooth muscle cells and pericytes), increase of vessels' lumen and reduction of fluidic resistance, r. This model includes two negative feedback mechanisms. The first feedback comes from the self-reduction of vasodilative concentration at the absence of exogenous inputs. The second feedback accounts for the removal of vasodilative chemicals due to the increase in blood flow which stops further dilation of vessels. Following equations describe this dynamics:

$$\begin{aligned} \dot{S} &= -\kappa \cdot S - \gamma \cdot 1/r + \epsilon \cdot [\chi_E + \eta \cdot \chi_I], \\ \dot{r} &= -r^2 \cdot S. \end{aligned} \tag{14}$$

Here, κ is the self-decay rate of S, and γ is the fraction of vasodilative chemicals which are removed as a result of the increase in the blood flow. In the second equation, a quadratic term is introduced to account for the nonlinear effect of the smooth muscle cell relaxation. This nonlinear effect acts in the following way: when the concentration of vasodilators increases, if the resistance of a vessel is closer to its minimum value, further dilation or reduction of the resistance is minimal. Conversely, if the resistance of a vessel is relatively high, a drastic dilation occurs when the vasodilator concentration increases. If we replace r with $1/F_{in}$ and use the blood flow response F_{in} as the state variable, we can rewrite the equation in a more plausible linear form:

$$\dot{F_{in}} = S. \tag{15}$$

Thus, the equation that incorporates the input becomes:

$$\dot{S} = -\kappa \cdot S - \gamma \cdot F_{in} + \epsilon \cdot [\chi_E + \eta \cdot \chi_I]. \tag{16}$$

3) M_2 Dual-Pathway Model: Based on the hypothesis of the unified theory and our observations, the evoked blood flow response is likely to have two main working mechanisms (acute and delayed) each with a distinct rate constant and sensitivity. Longden et. al. reported that the acute pathway only employs the smooth muscle cells. This means the acute pathway only affects arteries and arterioles [4]. On the contrary, the delayed pathway activates both smooth muscle cells and pericytes [5]. To formulate these dynamics, we propose a model with two distinct pathways, where each pathway has two state-space variables. Even though acute response does not follow the same physiological process similar to the delayed response, we found that a similar two-state model, with different time constants, can mimic the shape of the acute response reasonably well.

For the acute pathway, we consider the acute vasodilative molecule concentration S_A and its blood flow response F_A as state variables. The relationship between these two state variables and inputs are:

$$\begin{aligned} \dot{S_A} &= -\kappa_A \cdot S_A - \gamma_A \cdot F_A + \epsilon_A \cdot [\chi_E + \eta \cdot \chi_I], \textit{and} \\ \dot{F_A} &= S_A. \end{aligned} \tag{17}$$

Here, all rate constants are labeled with a subscript A. It is clear that in this approach, the acute pathway, by itself, has a dynamics similar to the M_1 model formulated by the equations 15 and 16. Similarly, we can consider two state variables for the delayed pathway (delayed vasodilative molecule concentration S_D and delayed blood flow response F_D) and use the same set of equations to formulate the dynamics:

$$\begin{aligned} \dot{S_D} &= -\kappa_D \cdot S_D - \gamma_D \cdot F_D + \epsilon_D \cdot [\chi_E + \eta \cdot \chi_I], and \\ \dot{F_D} &= S_D. \end{aligned} \tag{18}$$

Therefore, the total blood flow response, F, is the superposition of both acute and delayed blood flow responses.

$$F = F_A + F_D. \tag{19}$$

4) M_3 Nonlinear Dual-Pathway Model: The delayed response is likely to be conducted through molecular diffusion process [5], which is a nonlinear process. To represent this dynamic in our model, we include a nonlinear function in the feedback path of the delayed pathway. To emulate the non-linearity of evoked CBF response, we inserted sigmoid functions, $erf(x) = \frac{2}{\sqrt{\pi}} \int_0^x e^{-t^2} dt$, into both pathways of the M_2 model, Figure 2c. For the acute pathway, the non-linearity is inserted at the output stage. For simplicity, we keep the notation for the acute pathway output as F_A but we adopt an intermediate state variable F'_A to write the equations as follows:

$$\begin{aligned} \dot{S_A} &= -\kappa_A \cdot S_A - \gamma_A \cdot F'_A + \epsilon_A \cdot [\chi_E + \eta \cdot \chi_I], \\ \dot{F'_A} &= S_A, \\ F_A &= erf(F'_A \cdot \alpha_A)/\alpha_A. \end{aligned} \tag{20}$$

For the delayed pathway, we have inserted the sigmoid function into the feedback path of F_D. Therefore, the delayed dynamics is modeled by:

$$\begin{aligned} \dot{S_D} &= -\kappa_D \cdot S_D - \gamma_D \cdot F'_D + \epsilon_D \cdot [\chi_E + \eta \cdot \chi_I], \\ \dot{F_D} &= S_D, and \\ F'_D &= erf(F_D \cdot \alpha_D)/\alpha_D. \end{aligned} \tag{21}$$

The insertion of the sigmoid function dampens the magnitude of the negative feedback and slows down the removal rate of the delayed vasodilators, S_D. Since sigmoid function saturates when a relatively stronger input occurs, this function damps the output (blood flow feedback F'_D) further compared to smaller inputs. As a result, it takes longer for the CBF response to decay. Parameters α_A and α_D tune the non-linearity of sigmoid functions.

D. Simulation

We used the mathematical framework of the optical stimulation model, two-state neuron model and M_3 nonlinear dual-pathway NVC model to run a set of simulations.

Figure 4a-d shows the transition of channel states when a train of blue light pulses is applied for optogenetic stimulation. Based on this simulation, both excitatory and inhibitory cell populations are activated in the process which is shown in the trace of the state variables χ_E and χ_I. As displayed in Figure 4e, at first, a relatively large spike occurs in the value of χ_E, which is subsequently suppressed by the activation of inhibitory cells, χ_I. Both χ_E and χ_I eventually reach to steady-states. The detected LFP is the superposition of induced field potentials at the proximity of the recording electrode caused by the photocurrent and the activity of both cell populations.

Stimulation by this pulse-train demonstrates how the equilibrium state is established in the model. The trained model (once parameters are optimized) shows that the equilibrium state is the result of the balance between three quantities: state of activity in inhibitory and excitatory neurons and the photocurrent. Meanwhile, the activity of inhibitory neurons contributes to the rebound signal, while the photocurrent and the activity of excitatory neurons contribute to the downward deflection in the LFP signal, Figure 4d-f.

The optogenetic stimulation in this example evokes hemodynamic responses on a longer timescale. When neurons fire, both χ_E and χ_I contribute to the process of neurovascular coupling. The acute component has a faster rate-constant and ends in about $6.0sec$. The delayed component has a slower rate constant compared to the acute response and comes to end in about $30.0sec$. Both acute and delayed responses appear as damped oscillators. The superposition of outputs from these two pathways constitutes a biphasic CBF response with two distinct peaks as displayed in Figure 2k.

III. Experimental Setup and Data Acquisition Protocols

A. System Design

Schematic of the optical setup that we developed and used in this work is displayed in Figure 5a. The setup is made of two optical paths, one for the spectral-domain optical coherence tomography (SD-OCT) and a second path for optogenetic stimulation. The SD-OCT scanner uses a $1310nm$ light source with $170nm$ bandwidth which produces $10mW$ of optical power to perform broadband interferometry and Doppler velocity measurements. This imaging branch provides $\sim 4.4\mu m$ axial, and $\sim 5.1\mu m$ lateral resolution, $5mm^2$ field of view at the maximum speed of $80k$ A-scan/sec. Via periodic time-sharing, the scanner can monitor cross-sections of up to 5 discrete vessels of diameter $\leq 100\mu m$ at the maximum total frame-rate of $200f/sec$ with negligible aliasing artifact. To add the second path to the setup, we included a custom-made relay lens (combination of a scan lens, SL1, and a tube lens, TL1) to the optical path of the SD-OCT scanner [14]. The relay lens extends the distance between the SD-OCT galvanometer, GM1, and the objective lens, OL, and we used this space to integrate a dichroic mirror, D1, to separate infrared wavelengths of the SD-OCT from the visible wavelengths we use for stimulation and fluorescence imaging.

A $15mW$ fiber-coupled $450nm$ blue laser (LP450, Thorlabs, NJ, USA) was installed on the setup for optogenetic

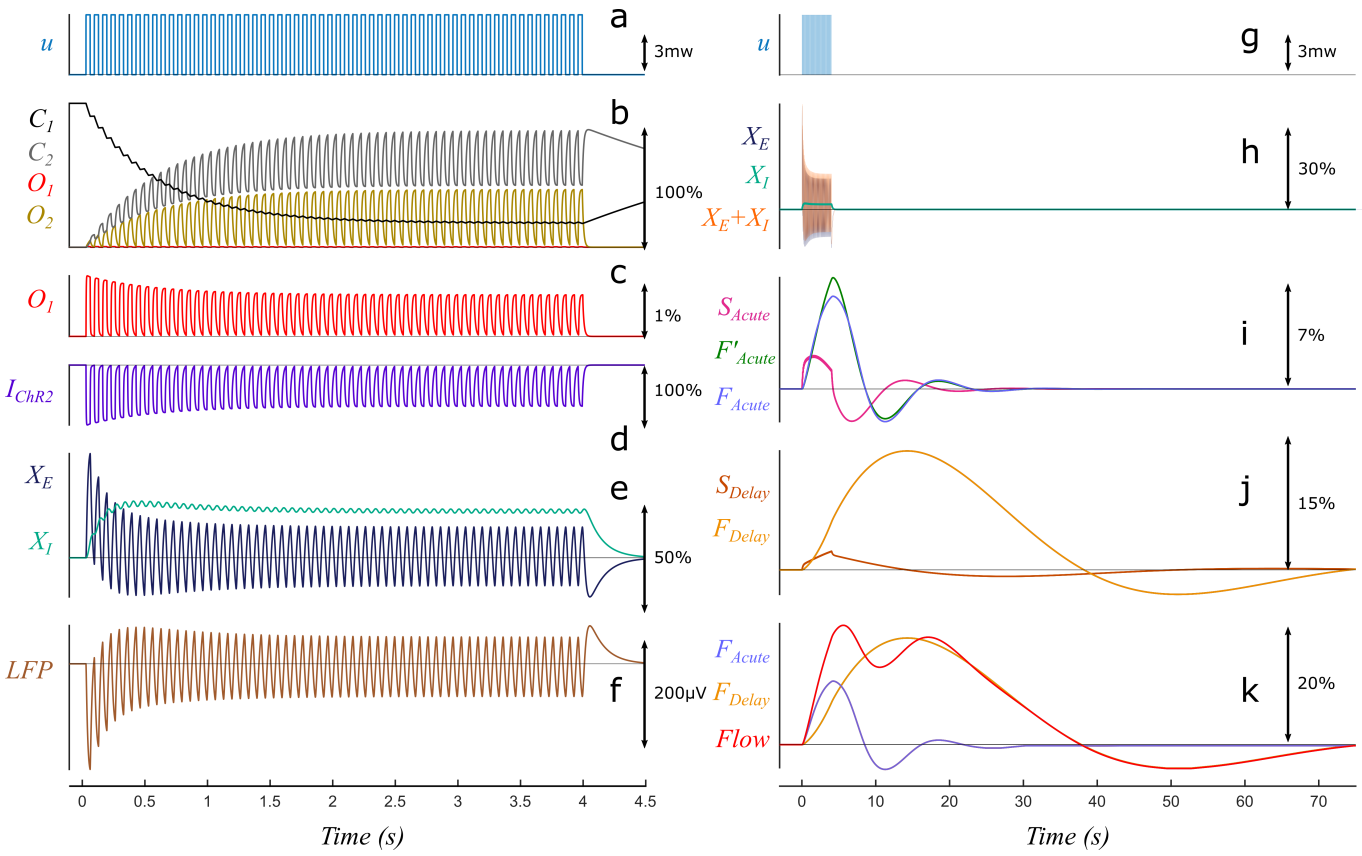


Fig. 4. Simulating the LFP and CBF responses to (a) a train of stimulating light pulses, (b,c) the developed model traces the transition of channel populations between the closed and open states, (d) generated photocurrent, (e) fluctuations in the activity level of excitatory and inhibitory cells, (f) induced LFP signal, (g,h) the stimulation pulses and neural activity in a longer time frame, (i-k) trace of the NVC state variables following optogenetic stimulation of excitatory neurons by the pulse train. The curves show temporal changes in the concentration of vasodilative chemicals and the corresponding CBF responses for both acute and delayed pathways.

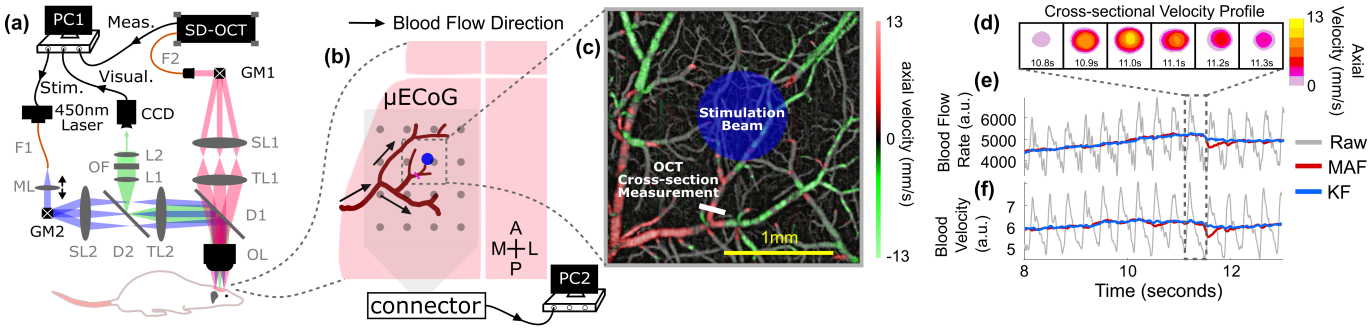


Fig. 5. The experimental setup combines optical coherence tomography (OCT), electrocorticography (ECoG) and optogenetic stimulation for concurrent CBF and LFP measurements as well as neural stimulation, (a) schematic of the setup that combines three optical paths by using two dichroic mirrors. The pink, green, and blue colored lines depict the path for the SD-OCT, optogenetic stimulation, and fluorescence imaging, (b) we implant transparent ECoG epidurally in each animal to record LFPs simultaneously, (c) fusion image of color-coded axial velocity measurements over the angiogram. The white line and blue circle show the vessel cross-section that is monitored by the SD-OCT and the selected area for optogenetic stimulation, (d) color-coded axial velocity B-scan of the vessel cross-section over time. A full cycle of heart pulsation from diastole to systole, (e) an example of CBF measurement (grey curve) obtained by locating a bounding box, which encapsulates the vessel cross-section shown in panel (d), and adding velocity values of all pixels inside the bounding box, (f) an example of blood velocity measures obtained by finding the maximum velocity value within the bounding box. Heart pulsation directly affects DCT measurements. A moving average (MA) filter (black curve) or an extended Kalman filter (red curve) was used to eliminate the effect of heart pulsation.

stimulation. This laser offers microsecond response time to the modulation signal which was essential to achieve the necessary temporal resolution when generating stimulation pulses. A programmable galvanometer, GM2, was added to the optogenetic path of the setup to produce arbitrary 2D patterns of neuro-stimulation. A second relay lens mechanism (combination of SL2 and TL2) was included to open some space for a second dichroic mirror, D2, to add a side branch for simultaneous fluorescence imaging. The system allows controlling the position, intensity, and duration/duty-cycle of the stimulating laser pulses. Also, by repositioning the movable lens, ML, we could control the beam size on the tissue. In our experiments, we were repositioning this lens to achieve different spot sizes changing between $266\mu m$ and $800\mu m$ in diameter. During experiments, first, we were scanning the cortex to generate a 3D angiogram. The produced angiogram was then used to select a group of vessels to be monitored closely for their reactions to optical stimulation. Figure 5c shows a typical angiogram in which velocity measurements are shown by color codes. Cross-section of one selected vessel in which the velocity profile is color-coded for multiple snapshots at different phases of a cardiac cycle is displayed in Figure 5d.

B. Data Acquisition and Processing

The detailed recording protocol of this work was adopted from our previous publications [11], [13]. In our practice, to measure axial blood velocity in each vessel, we were scanning the cross-section of a selected vessel and then we were using the Szkulmowski's high sensitivity method to measure the axial velocity $V_a(z, x, t)$ at time t and depth/lateral coordination z/x [30]. To remove the distortion caused by the tissue structural heterogeneity from this value, we were making this measurement twice, once through the forward pass and a second time during the return pass when the galvanometer was returning the beam to the scanning start point. What was saved at the end was the average of these two measurements. In the next step, we were applying a smoothing filter of size 3×7 along z and x directions to reduce the noise and obtain the filtered velocity profile $V_s(z, x, t)$. To compute the axial *blood-flow index*, we were adding values of filtered axial velocities over the cross-section of the vessel under test. Therefore,

$$BF_a(t) = \sum_{z,x} V_s(z, x, t). \tag{22}$$

Figures 5e,f show the evolution of the blood flow index during a typical neural stimulation. Blood flow in all vessels is modulated by cardiac pulsations. Breathing cycles also cause some fluctuations in blood flow measurements which are usually at the same order of magnitude compared to the evoked blood-flow response caused by stimulating nearby neurons. Therefore, to accurately measure CBF, we needed to eliminate these artifacts. For this purpose, we implemented an extended Kalman (EK) filter and a length-locked moving-average (MA) filter, Figures 5e,f. The EK filter was continuously estimating contributions of the cardiac pulsation, BF_c, and respiratory harmonic, BF_r, to the recorded CBF. Therefore, the recorded CBF was the superposition of three terms: BF_c, BF_r and a relatively slow-varying trend, BF_e, in which the NVC effect is embedded.

$$BF_a(t) = BF_e(t) + B_c(t) + B_r(t). \tag{23}$$

For the implementation of the discrete MA filter, the length of the filter, $N_c(m)$, was locked to an integer multiplication of the cardiac cycle period, $T_c(m)$. Typically, $T_c(m)$ was taking values within the interval $[0.13 - 0.2]sec$. The length-locked mechanism had the benefit of reducing the aliasing effect while introducing only some negligible delay. The smoothed flow index was calculated by:

$$BF_e(t) = 1/N_c(m) \cdot \sum_{i=1}^{N_c(m)} BF_a(t - i), \tag{24}$$

$$N_c(m) = M \times T_c(m),$$
$$M \in [5 - 10]. \tag{25}$$

The cardiac cycle period, $T_c(m)$, was determined experimentally by finding the maximum peak frequency in the power spectral density of BF_a. In this notation, m indicates the index of latest updates. We found that the cardiac cycle period is reasonably stable over $5sec$ periods but needs to be updated every $5sec$. The percentage change in the blood flow response, $BFR(t)$, was calculated by:

$$BFR(t) = \frac{BF_e(t) - BF_b}{BF_b} \times 100\%, \tag{26}$$

where BF_b is the baseline blood flow and it is defined as the time-averaged BF_a measured from the signal prior to the start of stimulation. BFR reflects relative changes in the actual blood flow of a vessel cross-section and it is not sensitive to scanning parameters or the physical orientation of the vessel. To eliminate the effect of physiological fluctuations, in practice, we were recording $BFR(t)$ multiple times to produce the ensemble average of the CBF response, $\widehat{BFR}$.

C. Model Parameterization

The collected experimental data was used to tune parameters of the model. We used optimization algorithms to minimize the sum of square of errors defined as the difference between the acquired LFP signals and blood flow measurements and predictions of the model over all recorded sample points.

$$\mathbf{p} = argmin \sum_i \left[F(i) - \hat{F}(i, \mathbf{p})\right]^2. \tag{27}$$

Here, i is the index of a sample point and $\mathbf{p}$ is the vector of parameters. A typical gradient descent algorithm was used to search for the optimal parameter vector. F and $\hat{F}$ are measured and model estimated values, respectively, for either the LFP or blood flow responses.

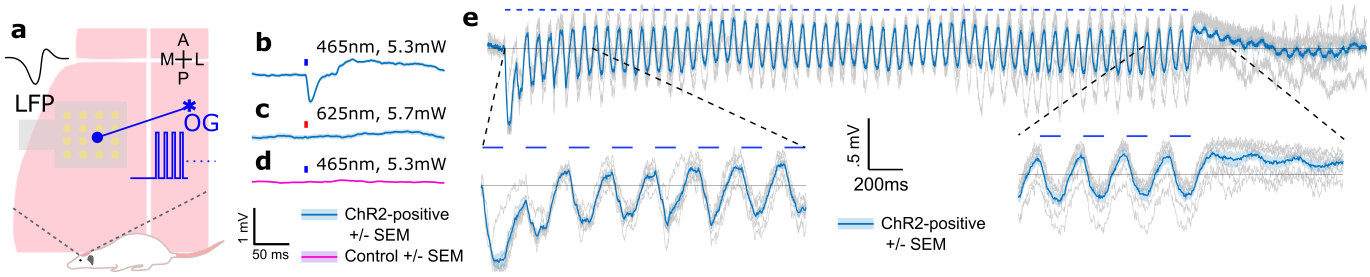


Fig. 6. Characteristics of optogenetically evoked LFPs responses, (a,b) ChR2+ mice were responsive to blue light stimulation ($1ms$, $465nm$, $5.3mW$) ,and recorded LFPs included a fast downward spike and a slow upward trend, and they were in close correlation with the stimulation pulses, (b,c) we observed no noticeable LFP signal when we exposed the brain of a ChR2+ mouse to red light ($625nm$, $5.7mW$) or when we exposed the brain of a wild-type mouse to blue light pulses ($n = 2$), (d) to generate CBF responses, we used sustained $1sec - 12sec$ pulses of blue light stimulation ($15Hz$, 50% duty cycle). As shown, a $4sec$ stimulus could evoke consistent neural oscillations closely correlated to the stimulating pulses.

D. Animal Preparation

In this study, we used $6 - 14$ weeks old transgenic optogenetic mice (Thy1::ChR2/H134R-YFP, or Thy1::ChR2-YFP). Using transgenic animals simplifies the experimental procedures by bypassing the need to perform gene delivery via viral injection. Moreover, the expression of opsins and light sensitivity is relatively uniform over the entire cortex in transgenic animals which is an essential factor in this research.

All procedures were carried out in a facility accredited by the Association for Assessment and Accreditation and Laboratory Animal Care (AAALAC) and approved by the University of Wisconsin Institutional Animal Care and Use Committee (IACUC) and conducted within the ethical guidelines of the National Institutes of Health (NIH).

For the acquisition of optogenetically evoked LFP signals, each animal was receiving a transparent ECoG array under a cranial window. The reference wire of the ECoG was attached to an area of the thinned bone on the other side of the sagittal suture. Details of the surgical procedures are available in [17]. For the first round of experiments, we were placing a $465nm$ blue light emitting diode (LED) $20mm$ above the tissue to expose $3mm$ in diameter area of the somatosensory cortex to $5.3mW$ (at maximum) optical power through the cranial window and transparent ECoG. Prior to experiments, mice were sedated via injection of ketamine ($75mg/kg$ SC) and dexmedetomidine ($25\mu g/kg$ SC) and supplied with oxygen and a heating pad. At the end of each experiment mice were recovered by reversing the dexmedetomidine with atipamezole($0.5mg/kg$ SC).

The collected LFP signals were processed offline by first averaging across trials and then low-pass filtering at $500Hz$. In some experiments (e.g., stimulation by chirped pulses), LFP signals were also high-pass filtered ($1.3Hz$ cut-off, 4th order IIR Butterworth) to remove the drifting of the baseline that is potentially caused by some uncorrelated activities.

For the development of the NVC model, experiments were conducted on the SD-OCT platform. In those experiments, we applied blue laser pulse-trains of $450nm$ wavelength with different durations, duty cycles, or light intensities, while we were recording CBF responses from a set of selected cortical arteries. Prior to experiments, animals were sedated with isoflurane ($1.5 - 2.0\%$ oxygen) and were administered by $0.25mL$ of fluids (sterile saline solution 0.9% and dexamethasone $2mg/kg$). The scalp was retracted, and the skull on top of the somatosensory cortex was thinned over an area of about $3.0mm$ in diameter and a microscope coverslip of the same size was installed. The anesthetic was switched to ketamine (25 - $100mg/kg$ SC) and dexmedetomidine (0.05 - $0.5mg/kg$ SC) during the experiments.

In some animals, before starting the imaging session, we were first acquiring the LFP data. For these experiments, after thinning the skull and before installing the coverslip, a transparent ECoG was implanted over the region of interest and gel-foam was applied around the device to maintain the moisture of the skull. When the LFP recording was completed, to prepare the animal for imaging, we were first removing the ECoG and then installing a coverslip. Same as before, recorded LFPs were processed offline; however, this time, three 3rd order IIR Butterworth filters were used sequentially to process the data including a low-pass filter (cut-off frequency $60Hz$), a high-pass filter (Cut-off frequency $3Hz$), and a band-stop filter (stop-band between $55Hz$ -$65Hz$).

IV. Experiments

A. Characteristics of Local Field Potentials

To develop our model of NVC based on the data acquired during in-vivo experiments, we began by modeling the effect of optogenetic stimulation on LFPs, Figure 6a. In these experiments, we used transgenic Thy1::ChR2-YFP mice which provide ubiquitous expression of ChR2 opsins in pyramidal neurons of cortical layer V. Data showed that blue light stimuli ($465nm$, $5.3mW$) was causing a rapid downward deflection of LFP signals which was picked up by an ECoG electrode.

Since the delivered high energy blue light photons pass through the transparent electrode array to expose the tissue, electrodes could produce Becquerel photovoltaic signals that are closely correlated to stimulating light pulses. To exclude the contribution of these artifacts from the electrophysiology data, we conducted control experiments in which we delivered red light photostimuli ($625nm$, $5.7mW$) to ChR2 positive mice and blue light photostimuli ($465nm$, $5.3mW$) to wild type mice. The experiments proved that the contribution of photovoltaic effect to LFPs are insignificant, Figure 6b.

Under the sustained blue light stimulus ($15Hz$, 48% duty cycle, $32msec$ pulse width), we observed an initial large transient downward spike, Figure 6e. We also observed rebound

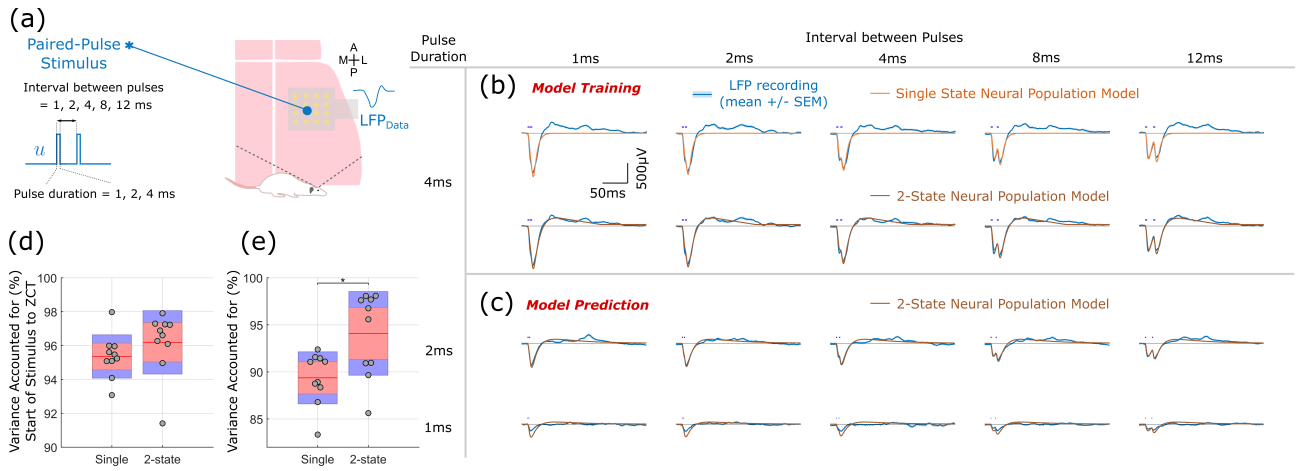


Fig. 7. Neuron model selection and validation, (a) a parametric paired-pulse experiment was performed to compare the performance of the single-state versus two-state neuron models, (b) the LFP of paired-pulse stimulus revealed a rebound signal after the offset of light exposures which corresponds to the slow rate constant of inhibitory neural connections. We used the data from $4msec$ stimulation duration experiment to train our model. From this test we learned that the single-state model in which only the excitatory neural activity is taken into account as a state variable can emulate the downward deflection of the LFP signal but not the inhibitory rebound compared to the two-state model which takes the activity of both cell populations into consideration, (c) the trained model was used to estimate the shape of the LFP for the $1msec$ and $2msec$ stimulation duration experiments under 5 different pulse intervals. The variance accounted for (VAF) is calculated based on each stimulation setting. (d) shows VAFs of two models for the time window between stimulation onset and the zero-cross-time (ZCT). The result shows the negative part of the LFP signal is accounted in both models, (e) VAFs for the entire LFP recording. We found that only the two-state neuron model can accurately capture the positive part of the signal. Here, ZCT indicates the moment when the signal crosses zero after the stimulus ends.

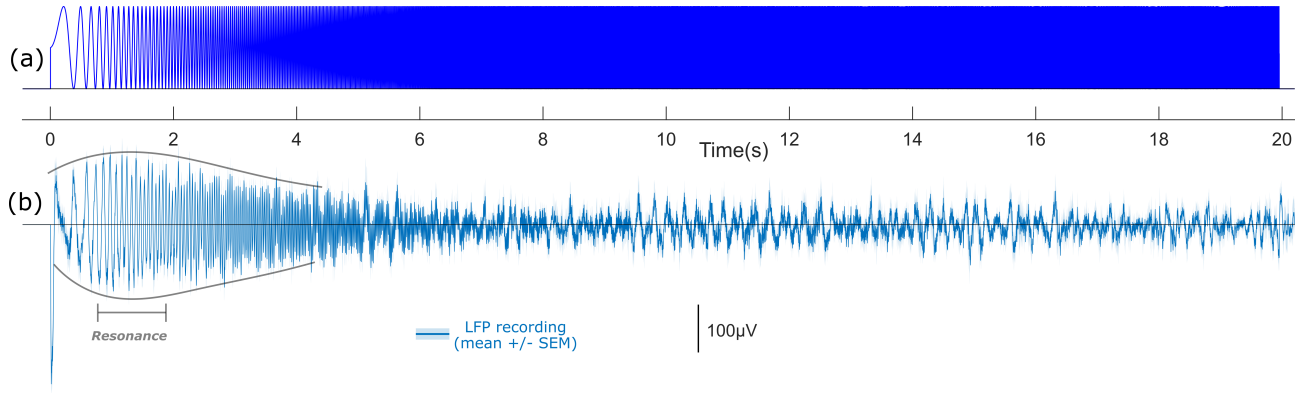


Fig. 8. Spectral analysis of optogenetically evoked LFP: To effectively activate neural oscillation, we need to measure the sensitivity of neurons to various stimulation frequencies, (a) we stimulated the tissue by a linearly chirped stimulus that sweeps frequencies ranging from $0.5Hz$ to $200Hz$, (b) collected data showed that stimulation frequencies within the range of $12HZ$ - $16Hz$ evoke resonance in the activity of exposed neurons.

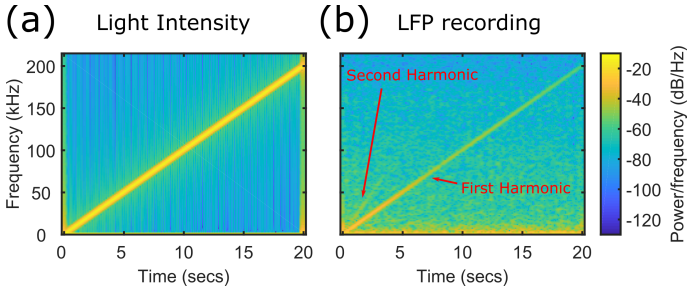


Fig. 9. Spectrograms of the chirped stimulating light pulse and the corresponding LFP.

signals within each stimulus interval which was surpassing the baseline. Meanwhile, as the train of light pulses continued, the LFP signal started oscillating around a slowly rising trend while the amplitude of oscillation was decreasing. After about $200msec$, the rising trend ceased and an equilibrium state was reached. When we stopped the stimuli, we observed a large rebound signal. The rebound signal then receded back to the baseline with a large time-constant potentially caused by the activity of inhibitory cells (decay time of $500msec$-$1000msec$) [31], [32]. Over the rebound signal, we observed a persistent $15Hz$ oscillation that continued even after the stimulus offset.

B. Neuron Model

To select the appropriate neuron model, we applied paired-pulse light stimuli and evaluated the performance of the one-state and two-state models in predicting the form of the induced LFP signals, Figure 7a. For experimental procedures see [17]. We tested all different combinations of $1msec$, $2msec$, and $4msec$ pulse durations and $1msec$, $2msec$, $4msec$, $8msec$, and $12msec$ pulse-to-pulse intervals at two

different intensity levels. After training both models by optimizing parameters using a portion of the collected data, we realized that the single-state model can capture the downward deflection but not the rebound signal that goes above the baseline during the recovery phase. However, the two-state model was able to capture both the downward deflection and the rebound signal, Figure 7b. In addition, the two-state model, could fairly predict the shape of LFP signals for other stimulation configurations which were not part of the training process, Figure 7c. Figures 7d, e provide the statistics from our model validation tests.

C. Spectral Analysis of Local Field Potentials and LFP Model Validation

To examine the system under different stimulus frequencies, we recorded LFPs while stimulating the tissue by a $20sec$ long linearly chirped blue light exposure sweeping frequencies from $0.5Hz$ to $200Hz$, Figure 8a. The generated LFP contains a consistent sinusoidal waveform ranging from $0.5Hz$ to $200Hz$ similar to the stimulation, Figure 8b. As shown in the figure, the envelope of the LFP signal has larger amplitude at the beginning but the amplitude of oscillations decreases at higher frequencies. When the temporal frequency goes above $60Hz$ (at $6sec$), the intrinsic neural noise becomes the dominant factor in the time trace.

Spectrograms of the stimulation pulse and the recorded LFP are shown in Figure 9. Here, we see that the stimulation energy ramps up at the rate of $10Hz/sec$ which is the same for the main harmonic of the LFP. Nonetheless, the LFP spectrogram has a second harmonic which ramps up at $20Hz/sec$. When we focus on short-time windows of the LFP signal, we can observe a consistent sinusoidal waveform that goes up to $200Hz$, Figure 10. By comparing the timing of the downward peak of the stimulation light and the upward peak of the LFP, we can detect a 180 degree phase difference between the stimulus and the LFP at low frequencies, Figure 10, and this phase shift increases at higher frequencies. The gain and phase-delay information for this signal are summarized in the Bode plot which shows the empirical transfer function from light intensity to LFP, Figures 11a,b. For one decade of frequency increase, we observe gain attenuation of $20dB$ and close to 180 degree phase delay. The low coherency that we observe around $90Hz$-$100Hz$ is caused by some form of nonlinearity in the system, Figure 11c. We used data samples from the first $2sec$, $10sec$ and then $20sec$ of the recorded LFP to train the model separately and we observed that the model when tuned by this data can predict and capture several features of the LFP signal including the shape and magnitude of the gain envelope, phase delay, and post-stimulus rebound that we observed in these time traces, Figure 11d. After tuning the model with this experimental data, when we analyzed the model, we realized that the ChR2 model has developed characteristics of a low-pass filter with the cut-off frequency of $\sim 20Hz$, while the neuron model has a resonance peak at $\sim 12Hz$ in its gain, Figures 11e,f. This resonance is directly related to the peak oscillation amplitude which was noticed before in the time trace of the LFP signal displayed in Figure 8b.

To explore and see how the equilibrium state is established, we conducted an experiment in which the brain was stimulated by a train of light pulses as shown in Figure 12a. Experiment was repeated for three duty-cycles (16%, 32%, and 48%) while the pulse train was applied for $4sec$. The model which was trained by this dataset shows that the equilibrium state is the result of the balance between three quantities: the activity level of inhibitory and excitatory neurons, and the intensity of the induced photocurrent. The activity level of inhibitory neurons is the main factor in the formation of the rebound signal while the magnitude of the photocurrent and the activity level of excitatory neurons shape the downward deflection.

To examine the accuracy of the model, we generated four trained parameter sets by using either the entire $4sec$ of the 48% duty-cycle stimulation pulse-train or just the first $2sec$ of the data from all three different duty-cycle tests, Figures 12. When tested, all four models were capable of predicting temporal features of LFP signals including the spike amplitude, recovery dynamics between stimulation intervals, post-stimulation rebound, and the slow rising trend.

D. Characterizing Optogenetically Evoked CBF Response

In this section, we examine the spatial and temporal characteristics of evoked CBF responses to optogenetic stimulation. As illustrated in Figure 13, the sustained pulse train of optogenetic stimulation causes a population of neurons in somatosensory cortex to fire and the surrounding vasculature to dilate. There are two main questions regarding spatial characteristics of this dynamics. The first question is which nearby neural population, once stimulated, triggers the largest CBF response in a particular vascular cross-section? and, how the location of simulation affects the observed CBF response at a selected vascular cross-section. To answer these questions, we designed experiments to extract spatial sensitivity maps of vascular cross-sections as a function of the stimulation location. For this purpose, we conducted a set of experiments in which we were recording CBF response of a main cortical artery at its multiple branches while raster-scanning the stimulation location within a defined grid that is shown in Figure 13b. At each round of this experiment, stimulating laser pulses were delivered to the center of one of the 25 circular areas shown in this figure where the diameter of each circle was $\sim 400\mu m$. Our Monte Carlo light-tissue interaction simulations ([18], [19]) proved that because of the scattering, the effective stimulation area will be a disk of this size even when the stimulation is mainly delivered to the center of the disc. After recording CBF responses at four vascular cross-sections of the main cortical artery, the beam of the blue laser was moved to another circle to activate a different neural population. We randomized the order of selecting circles and repeated the experiment 7 times for every stimulation location.

The results are the sensitivity maps that are displayed in Figure 13c for each vascular cross-section. Within each map, traces of the trial-averaged CBF responses are plotted at the location of stimulation. For instance, the vascular branch in the left most map of Figure 13c shows that the maximum response happens when the stimulation is delivered

to the top-left circular region. After comparing sensitivity maps of vascular cross-sections to high-resolution vascular angiography (produced by the same OCT platform), we found that the maximum response occurs when stimulated neural population co-locates with the downstream capillaries of the vessel under test. Furthermore, when the neural population around a vessel's downstream capillary bed is stimulated, we can see a biphasic CBF response which is composed of both acute and delayed components. The shape and magnitude of both components are functions of the stimulation location. Based on our observations, the delayed response is more sensitive to the stimulation location.

We noticed that a stimulation at the proximity of a vessel downstream capillary bed evokes stronger delayed response, while the magnitude of the acute response to the same stimulation is less sensitive to the stimulation location. We also observed that rate constants of CBF responses are parameters that are independent of the stimulation location.

In another experiment, to characterize the intricate dynamics of the biphasic CBF response, we stimulated the area close to a vessel's capillary bed with a laser pulse train but in each round we changed the duration of the stimulation from $1sec$, to $2sec$, $4sec$, $8sec$, and $12sec$, Figure 13d (4 animals, 9 vessel). This test was even repeated in wild-type animals where we used six times stronger optical power for stimulation and yet the recorded CBF response was negligible, Figure 13e.

The observed CBF response from this test demonstrated the interplay between acute and delayed components. Figure 14a compares the CBF responses to different stimulation durations. Here, peaks that are caused by the acute and delayed responses are marked by $\times$ and $\square$, respectively. We can see that for shorter stimulation durations ($1sec$, $2sec$, and $4sec$), the acute response is dominant and for the shortest stimulation durations the delayed signal is relatively invisible. Nonetheless, as we increase the stimulation duration, the delayed response becomes the dominant signal. For longest durations the two components merge and the biphasic form of the CBF is no longer visible.

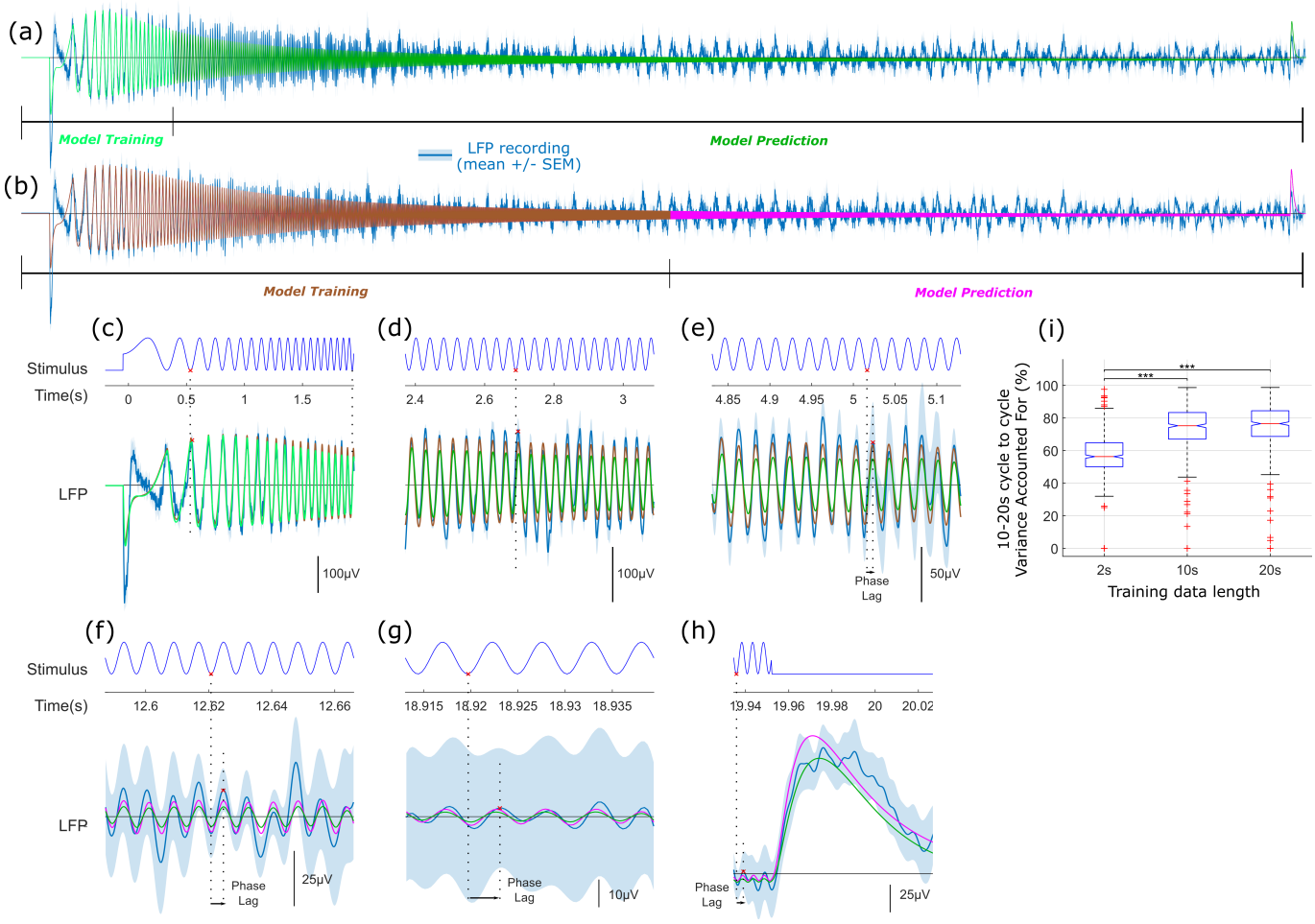


Fig. 10. Model validation and short-time window analysis of optogenetically evoked LFPs: (a,b) we trained the parameters of the models by using the the first $2sec$ and then separately $10sec$ of the recorded data. Both trained models could predict the oscillation magnitude and the post-stimulation rebound of the LFP signal, (c-f) short-time windows of experimental data and the model prediction. Points in figures marked by $\times$ indicate the initial 180^o phase differences at lower frequencies. As the stimulation frequency increases, the phase delay in the LFP signal grows as well, (g) at $180Hz$, we see more than 270^o of phase lag between the stimulus and LFP in both experimental data and the model prediction, (h) when the stimulation is turned off, a large but slow rebound signal appears which is potentially caused by the slow time-constant of the inhibitory neurotransmitters, (i) as the statistics show, with $10sec$ of training, the model could predict the rest of the response with reasonable accuracy. The variance-accounted-for (VAF) was calculated within each cycle and a fourth order polynomial function was used to remove unrelated neural noise which was causing baseline drifting.

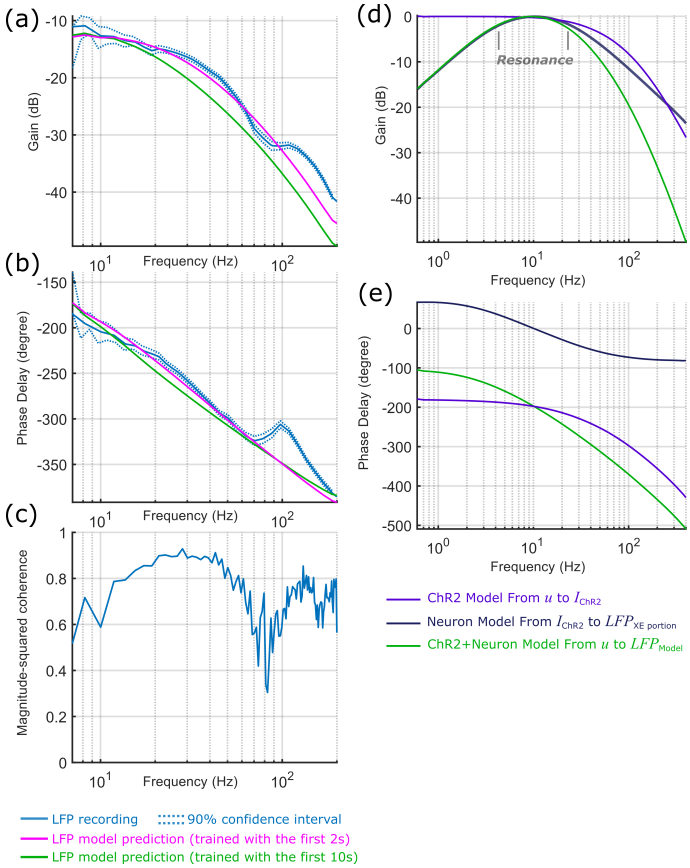


Fig. 11. Spectral analysis of LFPs evoked by chirp stimulation pattern: (a,b) in the frequency domain, the transfer function of the recorded LFP and trained models, from light intensity to LFP response, behave as low-pass filters, (c) the magnitude-squared coherency graph shows the recorded data has sufficient linearity across the tested frequencies, (d,e) we examine the transfer function of each model and noticed a resonance effect between $12Hz$ to $16Hz$ in both experimental data and the model output. We believe that this resonance is the result of the interaction between the excitatory and inhibitory neural populations.

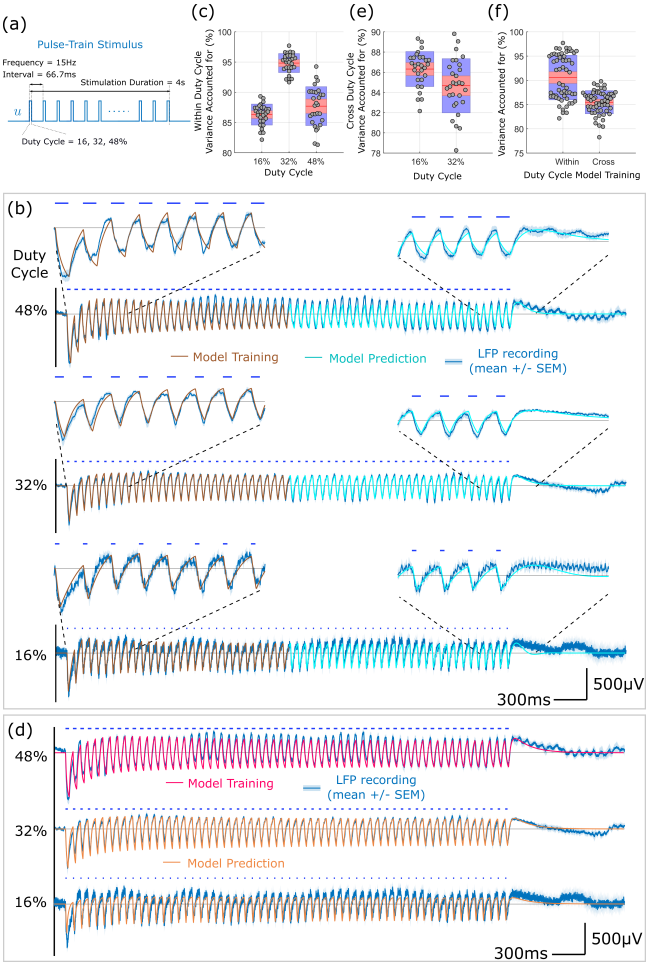


Fig. 12. TModel precision tests: (a) train of light pulses of different durations and duty-cycles were used to stimulate the brain tissue, (b,c) we considered two approaches to evaluate the model. In the first approach, LFP signals were recorded and the first $2sec$ of the data were used to train the model. Next the trained model was used to reproduce the later $2sec$ of LFP signals and model predictions were compared to data points which were not used during the training. The prediction accuracy VAF was calculated based on intervals between pulses, (d,e) in the second approach, LFP recording with the experimental setting of 48% duty cycle was used to train the model and predicted the experimental setting of 16% and 32%, (f) there was no significant difference in predicting the dynamics across responses from different experimental settings or within the same experimental settings.

Detailed analysis of the acute and delayed responses are shown in Figure 14. Figures 14b-g show multiple features of the acute and delayed responses separately for various stimulation durations. For both responses zero-to-peak times increase monotonically as the stimulation duration increases from $1sec$ to $12sec$. We also considered the time between the stimulation offset and the peak moment and we found that for different stimulation durations, acute responses reach the peak one second after the end of stimulation, whereas delayed responses peak in about $15sec$ after the stimulation offset. When the delayed response fall under the baseline, it shows that activated vessels are constricting during the recovery process. To quantify the time it takes for this vasoconstriction to appear, we defined the term *response time* to be the time between the stimulation onset and the moment the CBF response crosses the baseline going from positive to negative values. The data shows that the response time increases from $30sec$ to $50sec$ as we increase the stimulation duration, Figure 14g. If we use the response time of the $1sec$ stimulation duration as a reference, we can see that the response time for longer stimulation durations increases semi-linearly as shown in Figure 14h. This semi-linear proportionality shows about $1.5sec$ increase in response time for every $1sec$ increase in stimulation duration.

By laying all traces of different durations in one graph, we found a steady initial increase that can be described by an exponential decay function (M_0 model) with a time constant of $15.9sec$, Figure 14j. The time constant was found through numerical optimization over all stimulation durations. Even this simplistic model can estimate the acute response with reasonable accuracy for the first $12sec$. The residue, calculated by subtracting the recorded CBF response from the exponential decay function, is shown in Figures 14 l, m which demonstrates the precision of the model. The rise in residuals appears in about $12sec$ after the beginning of the stimulus which suggests that a dynamics that is not taken into account in the $M0$ model has initiated around this point.

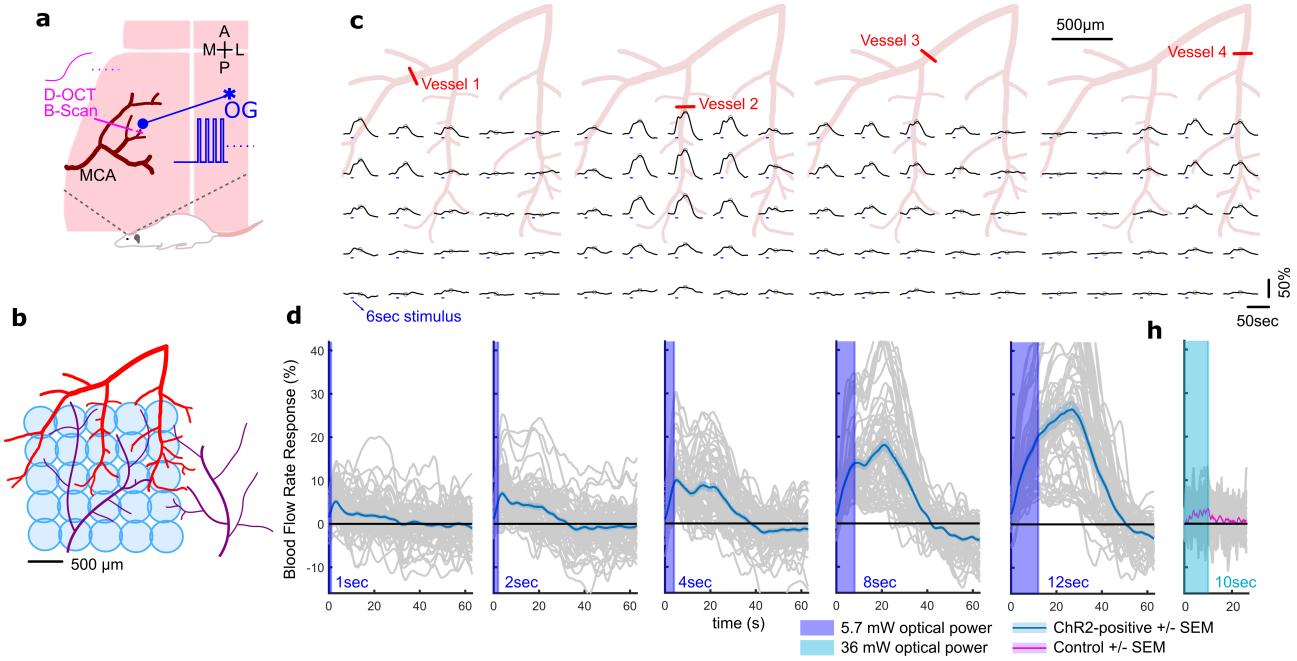


Fig. 13. (a) To induce noticeable CBF response that includes acute and delayed components, we used sustained $6sec$ stimulating pulses (15 Hz, 50% duty cycle) which was evoking consistent neural oscillations, (b) in this experiment, stimulation pulses were delivered to one of the 25 different locations marked by the grid of circles while the CBF response was being recorded at four vessel cross-sections, (c) the CBF response recorded at each vessel cross-section is shown as a function of the stimulation location. We observed strongest biphasic responses when we were stimulating confined regions close to the center of the feeding territory of each vessel, (d) we further evaluated acute and delayed components of CBF response with stimulation durations ($1sec - 12sec$). The data was rejected if the trial-averaged (7-9 trials) response showed insignificant difference between its baseline and post-stimulus response using paired t-test (4 of 13 vessels in 4 animals), (e) to verify that the response in ChR2 mice was not caused by heat, we applied the stimulus to wild-type mice but we made it six times more intense for this test. This stimulus level produces heat in the tissue and yet we found only a slight change in the vessel blood flow index.

This mechanism is basically the delayed response which has a magnitude proportional to the stimulation duration, Figure 14n.

In Figures 15 a, b we can see the trail-to-trail variance of the CBF response for multiple stimulation durations measured at a single vessel cross-section and averaged across seven trials, or for nine different vessel cross-sections and then averaged. The single vessel trial-averaged traces show similar dynamics to the cross-subject averaged traces, but with a smaller trial-to-trial deviation.

What we have learned from these experiments and the analysis can be summarized as follows: 1) in this dynamics the acute response peaks in about $1sec$ to $2sec$ after the offset of stimulus, 2) the time constant of the exponential decay is $\sim 15.9sec$, 3) the delayed response peaks in about $15sec$ after the end of stimulus, 4) the CBF response has a notch between the two peaks, 5) the CBF response has a post delayed-peak undershoot, and 6) the response time increases semi-linearly as a function of the stimulation duration (increasing at the ratio of $1.5sec$ for every $1sec$ increase in stimulation duration).

E. Modeling Optogenetically Evoked CBF Response

In the previous section, we studied main features and spatial-temporal characteristics of evoked CBF responses. We observed that the stimulation of neural population close to a vessel's downstream capillaries evokes the CBF response which has both acute and delayed components and we specifically analyzed the CBF response for stimulation pulses of different durations. In this section, we will study the performance of different NVC models, including M_1, M_2, and M_3 models, to see which model can reproduce all six features of the CBF response after tuning parameters of the model by using the data from experiments, Figure 16a,b.

Figures 16c, and d show the result of the training process as we optimized parameters of models to fit the model's output to the data and also we quantified the precision of the predictions for different stimulation intensities or durations. As discussed earlier, model M2 has a dual-pathway structure. Each pathway has two state variables and the model can reproduce the features (1), (2), (5), and (6) as listed in the previous section. Since the adopted linear model has a fixed response time, M2 model cannot reproduce features (3) and (4). To address this challenge, we modified the M2 model by adding a sigmoidal function in the feedback loop of the delayed response in the M2 model as shown in the block diagram of the M3 model. Because of this modification, the response time ratio and delayed-peak time were increased in M3 model and the model output matched the experimental data.

Previously, in Figures 4g-k, we showed the dynamics of the complete model when the system was stimulated by a pulse train. At the final stage of that simulation, Figure 4k, we observed that the acute response forms a notch between the two peaks (feature (6)), while the delayed response forms the post-delayed-peak undershoot (feature (5)).

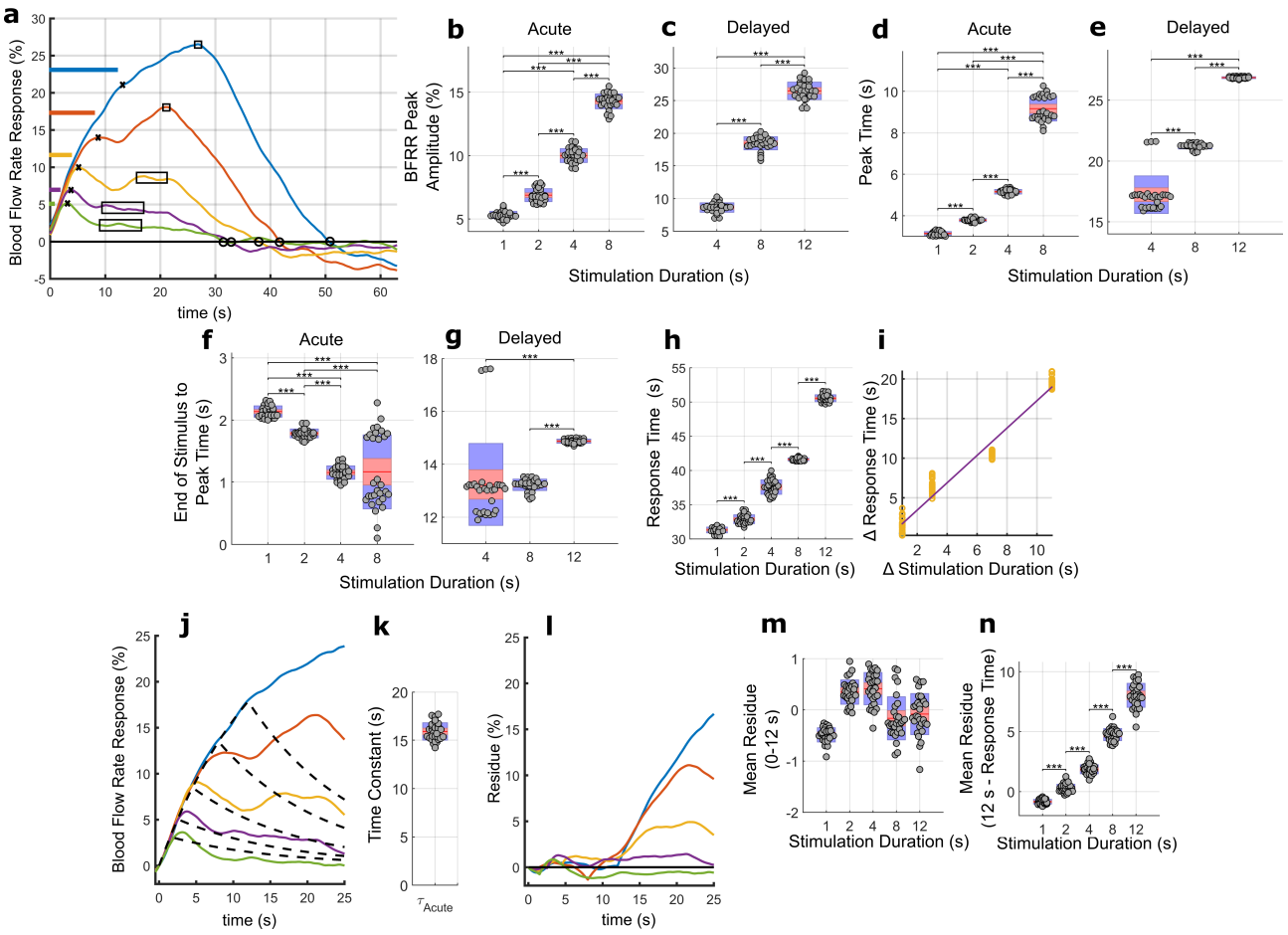


Fig. 14. Temporal feature analysis of CBF response. (a) overall CBF response for pulse train stimulation of different durations changing from $1sec$ to $2sec$, $4sec$, $8sec$ and $12sec$. We marked the following features in the data: time to reach the peak amplitudes marked by $\times$ for acute and by $\square$ for delayed responses, response-time marked by $\circ$ which is defined as the time between the stimulation onset and the moment the CBF response crosses the baseline from positive to negative. Statistics of acute and delayed components for: (b,c) CBF response amplitude, (d,e) time to reach the peak value, (f,g) the time between the end of stimulus and the time the CBF reaches the peak value. (h) response time plotted versus stimulation duration. We define response time as the time between the stimulation onset and the moment the CBF response crosses the baseline from positive to negative, (i) data shows that the response time increases semi-linearly as a function of the stimulation duration when the response of $1sec$ stimulation duration was considered the reference, (j,k) the exponential decay function with a time constant of $15.9sec$ captures the initial rise of the CBF response, (l) the difference between the observed data and the exponential decay function, (m,n) residual values which show the difference between the observed data and the exponential decay calculated for both the first $12sec$ and from $12sec$ to the time when response crosses zero. Bootstrapping method was used to resample the result from 9 vessels with 30 repetitions. Three asterisks indicate p-values ≤ 0.001.

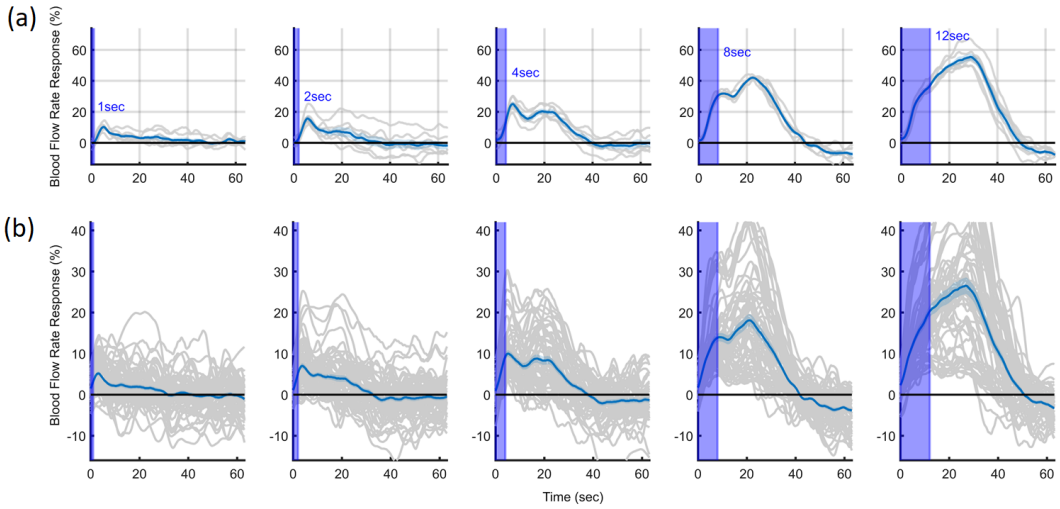


Fig. 15. The trail-to-trail variance of the CBF response under varying durations measured for: (a) a single vessel and averaged across seven trials, or (b) nine different vessels and then averaged.

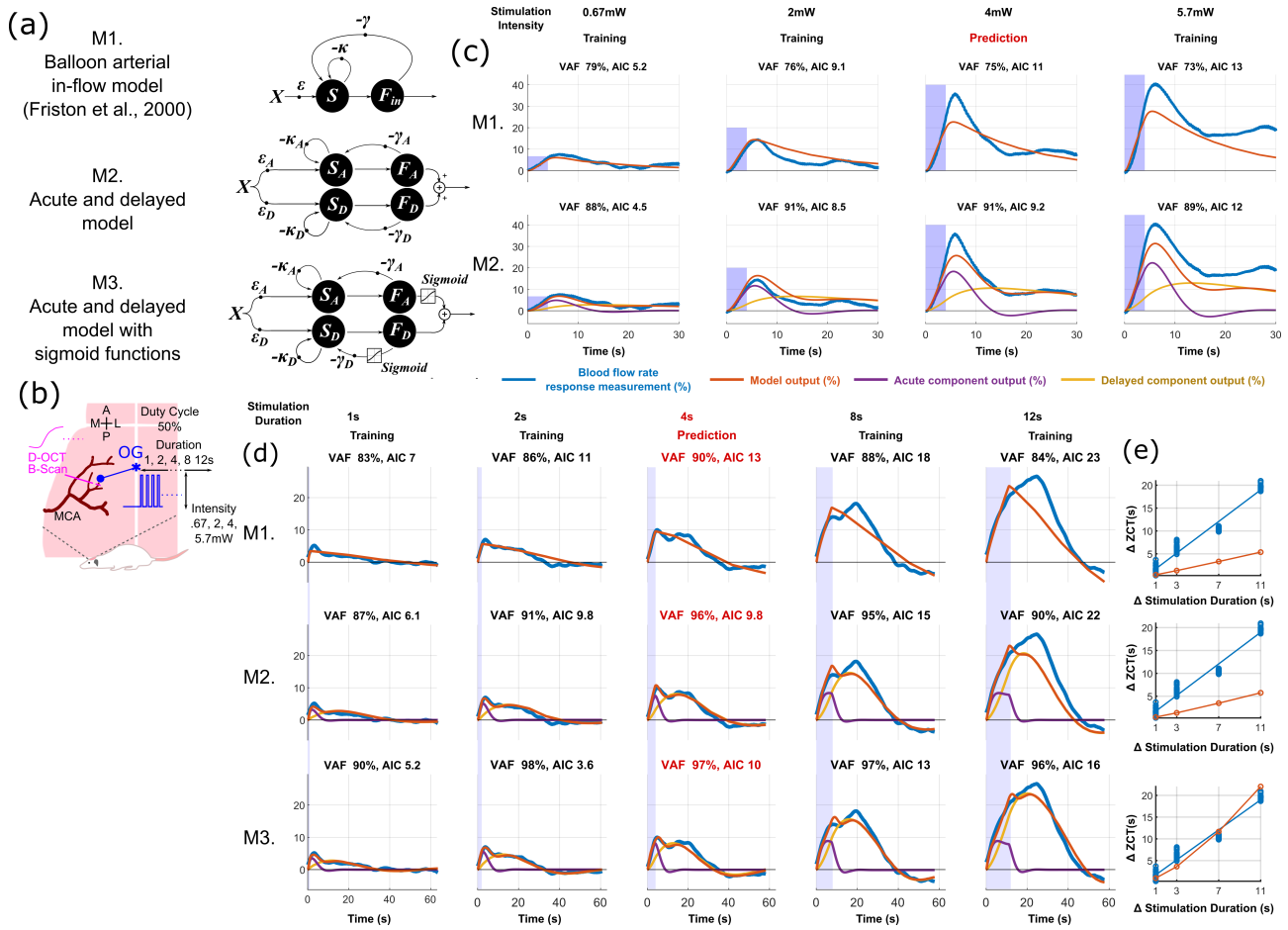


Fig. 16. (a,b) Neurovascular coupling model construction and validation. Three NVC models were investigated. We trained models with the experimental data for various stimulation intensities (0.67, 2, and $5.7mW$) and constant duration of $4sec$, (c) the trained model could predict the CBF response to the $4mW$ stimulus test. As shown, the M1 model can predict the acute response, but not the notch or the second peak. The M2 model can reproduce both peaks and the notch that is caused by the undershoot of the acute process, (d) when the M2 model was trained by the data in which we applied different stimulation durations, the trained model M2 could capture both peaks from the acute and delayed responses. Nonetheless, we observed some inaccuracy in reproducing the response time data, (e) to better replicate the experimental data and take nonlinearities into account, we created the M3 model in which sigmoid functions were added in the feedback loop of the delayed process and the output of the acute process. Two accuracy measures, VAF and Akaike information criterion (AIC), are reported.

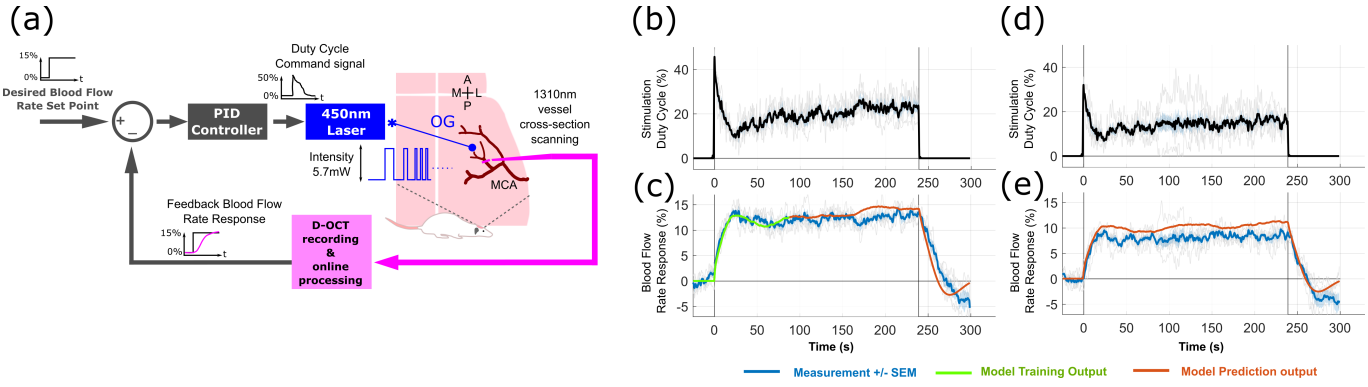


Fig. 17. (a) To investigate the consistency of the NVC process over time scales of several minutes, we conducted a set of closed-loop CBF control experiments. In this setup, a user defines a setpoint for the blood flow in a given vessel(s) and the closed-loop system continuously adjust the duration of optogenetic stimulation laser pulses to keep the blood flow close to the setpoint over the given period. The compensator here is a PID controller in which the feedback is provided by the SD-OCT imaging platform, (b-e) the setup could successfully maintain the CBF level of a selected vessel at 15% or 10% above the resting state when requested which indicates a degree of consistency in the NVC. To evaluate the consistency from a dynamic system perspective, we trained the model by using only the first $90sec$ of the data collected under the 15% setpoint experiment. After training, the model could predict the trajectory of the CBF response for the rest of the experiment and even its undershoot during the recovery phase. The trained model, with same parameters, could also predict the CBF response in the 10% setpoint experiment with some steady-state error.

F. Consistency of Neurovascular Coupling

To evaluate the consistency of the developed neuro-stimulation and NVC model (when the stimulation is lasting for longer), we arranged a set of closed-loop control experiments. One question we tried to answer was whether the early portion of the stimulation is more effective in triggering the CBF response or main features of the CBF response remain relatively unchanged if the stimulation sustains for a few minutes. In other words, we intend to test and see if we can detect any form of adaptation in the CBF response in a timescale of a few minutes. In our experimental setup, Figure 17a, we control the CBF in the vessel(s) under test by adjusting the activity level of nearby neural population via optogenetic stimulation. The goal of the system is to lock the CBF in the vessel(s) at arbitrary set-points for a given period of time. The feedback in this setup is taken from the SD-OCT system which continuously monitors the CBF in the vessel(s) through out experiments. The setup uses this feedback to form a proportional-integral-derivative (PID) controller and by readjusting the duration of stimulating laser pulses, it strives to keep the CBF close to the set-point for a duration of $240sec$. Details of the design of this PID controller are available in [11]. Results from this experiment showed that the controller could maintain the CBF over several minutes and remain stable.

In our next step, we trained parameters of the model by using only an early portion of the closed-loop control data. We hypothesized that if the underlying mechanisms controlling the NVC are plastic, then the prediction of the model, that is trained by the early portion of the data, should diverge from the actual CBF response as time passes. However, if underlying mechanisms are not plastic, then the model prediction should match the experimental data reasonably well for the entire period of the experiment. As shown in Figures 17b and c, the trained model could predict the closed-loop CBF response fairly well for the entire $240sec$ of data. The model which was trained with this dataset could even predict the CBF response for a different experimental setting as shown in Figure 17d, e. The model was successful in predicting many features of the CBF response signal including the rising of the signal and even the post-stimulus undershoot.

G. Characterizing Spatial Features of Optogenetically Evoked CBF Response

In the last section, after tuning the PID controller, we kept the parameters unchanged, but we tested the performance of the controller in closed-loop tests in other animals. We noticed that despite some fluctuations in the performance of the system going from one subject to another, in general, the closed-loop controller was reasonably successful in adjusting the blood flow level around the set-points. This again indicates that the rate constant with which the CBF is conducted remains consistent across subjects.

In our next step, we conducted a new set of experiments and evaluated the consistency of the rate constants in further detail. This is achieved by testing the dependency of the CBF response in a given vessel cross-section to stimulation pulses that are delivered to 25 different locations. Here, we were delivering optogenetic stimulating pulses to 25 different locations, marked by a grid of circles, as we were recording the CBF response at 4 different vessel cross-sections. This test was shown briefly in Figure 13 and repeated in more details in Figure 18. The hypothesis is that main features of neural stimulation and NVC model should remain the same as we change the location of stimulation. However, what can change as a function of stimulation location is the effectiveness of the stimulation in terms of triggering CBF responses. This dependency can be highly non-linear.

For this study, we used the data from this 100 trials (4 vessel cross-sections and 25 stimulation location, while the experiment was repeated 7 times) and we optimized the parameters. We found one set of parameter values which could replicate CBF responses including all main features of all trials, Figures 18c,d,e.

In our model, the evoked neural activity triggers the CBF response through two different paths for the acute and delayed responses. However, the coupling between neural activity and CBF response is a function of the location of stimulation. Moreover, we assume each of acute and delayed components of the response might have different efficiencies as a function of distance. We use the efficacy parameters, ϵ_A and ϵ_D within the developed model to incorporate such dependencies. Analysis of these two parameters can capture the spatial pattern of dependency of the CBF response to the location of stimulation. For instance, for the acute response, we used these 25 CBF responses to different stimulation locations to generate a matrix of efficacy values for each vessel. In other words, the efficacy parameter is elevated from a single value parameter to a sensitivity map which is represented by the efficacy matrix as shown in Figure 18f. A similar process was applied to the delayed response for every trial and we generated the efficacy matrix for the delayed response, ϵ_D. When these matrices were stored in the computer, the same model with the same parameter values could reproduce all spatial-temporal features of CBF responses in different vessels, successfully. This test suggests that the mechanism and parameters of evoked CBF responses are not plastic but stable.

As shown in the data, when the stimulated neural population is in the vicinity of downstream capillaries of a monitoring vessel, the CBF response is stronger. Here, for each vessel cross-section, we define *distance* as the euclidean distance between each stimulation location and the center of mass of the efficacy matrix. In Figure 18f, the center of mass for each map is marked by $\times$. The data shows that when this distance increases, the value of efficacy parameters reduce for both acute and delayed responses. Nonetheless, the delayed response usually decays faster, Figure 18g.

H. Possible Effect of Propagating Dilation to a Vascular Network

During our investigation of the temporal dynamics of evoked CBF responses, we encountered cases in which stimulation of neurons close to one vessel was causing some small reduction of blood flow and noticeable decrease in maximum

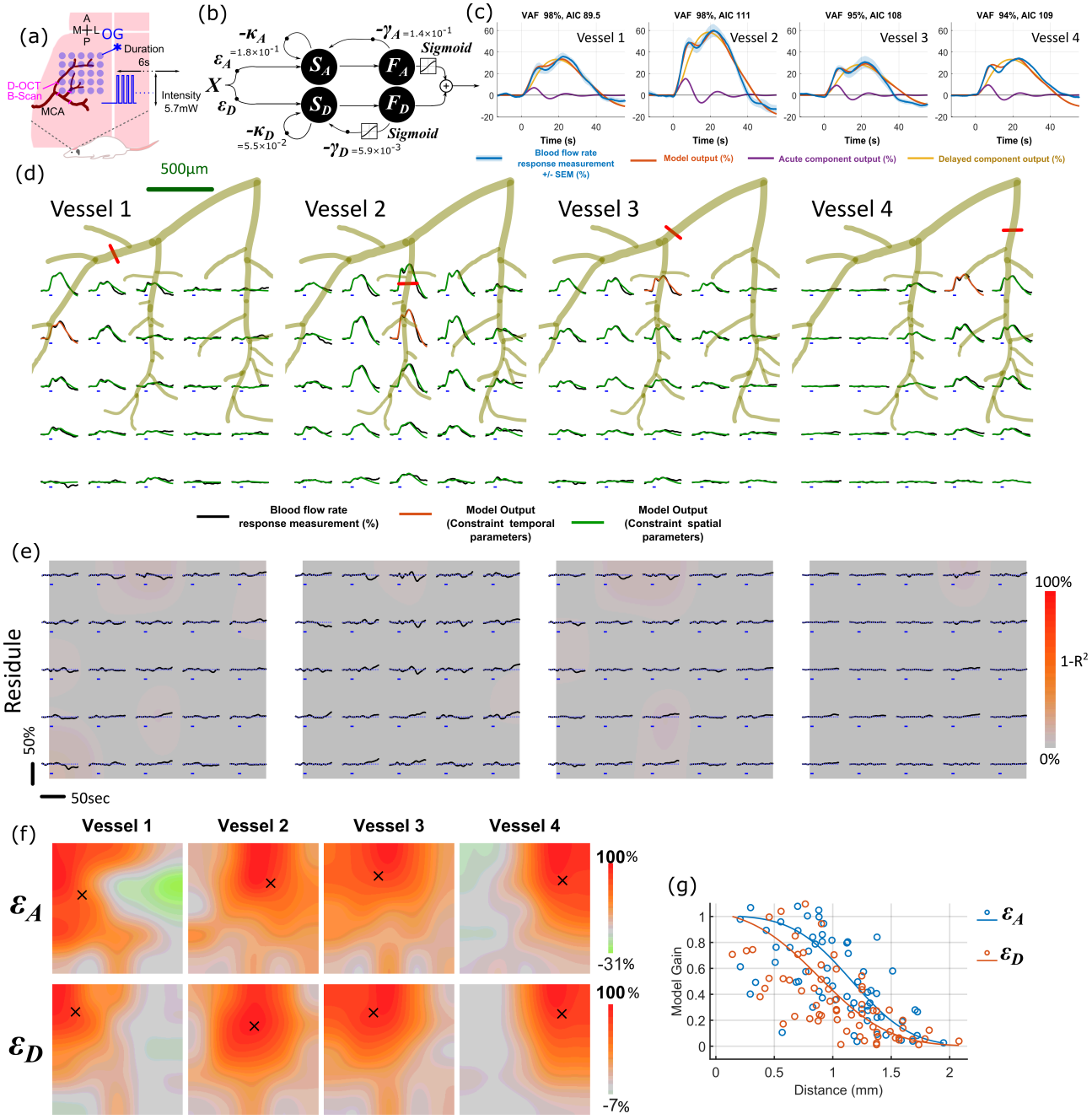


Fig. 18. CBF response as a function of neural stimulation location, (a) stimulation pulses were delivered to 25 different locations around four branches of a vessel while CBF responses in all branches were closely monitored by the SD-OCT platform, (b) we used the collected data to find one set of parameters for the model which could fit well to all these 100 data points, (c) to find this set of parameters, we first used the data generated by stimulating the location which had maximum sensitivity for each vessel and we optimized temporal parameters of model (i.e., κ_A, κ_D, γ_A, γ_D). While temporal parameters were fixed and were not changing as a function of stimulation location, we allowed efficacy parameters (ϵ_A, ϵ_D) to be optimized as a function of location, (d) we then applied the optimized temporal parameters to the rest of 96 responses and allowed efficacy parameters to be freely adjust. We found a degree of consistency in the temporal features for all responses, (e) data shows that the residue (defined as $100\% - VAF$) is less than 10%, (f) interpolated color-map images of efficacy parameters. Each matrix is normalized to its maximum values. $\times$ indicates the location of the center of mass in each map. In some cases, we observe reduction in blood flow which is caused by the activation of neighboring branches. This concept is shown by the negative values in these maps, (g) the curve shows the value of efficacy parameters as a function of distance between the center of mass and the location of stimulation. A parameterized Error Function ($erf(x)$), once optimized can reasonably fit the data. The data shows that the acute efficacy decays slower than the delayed efficacy as distance increases.

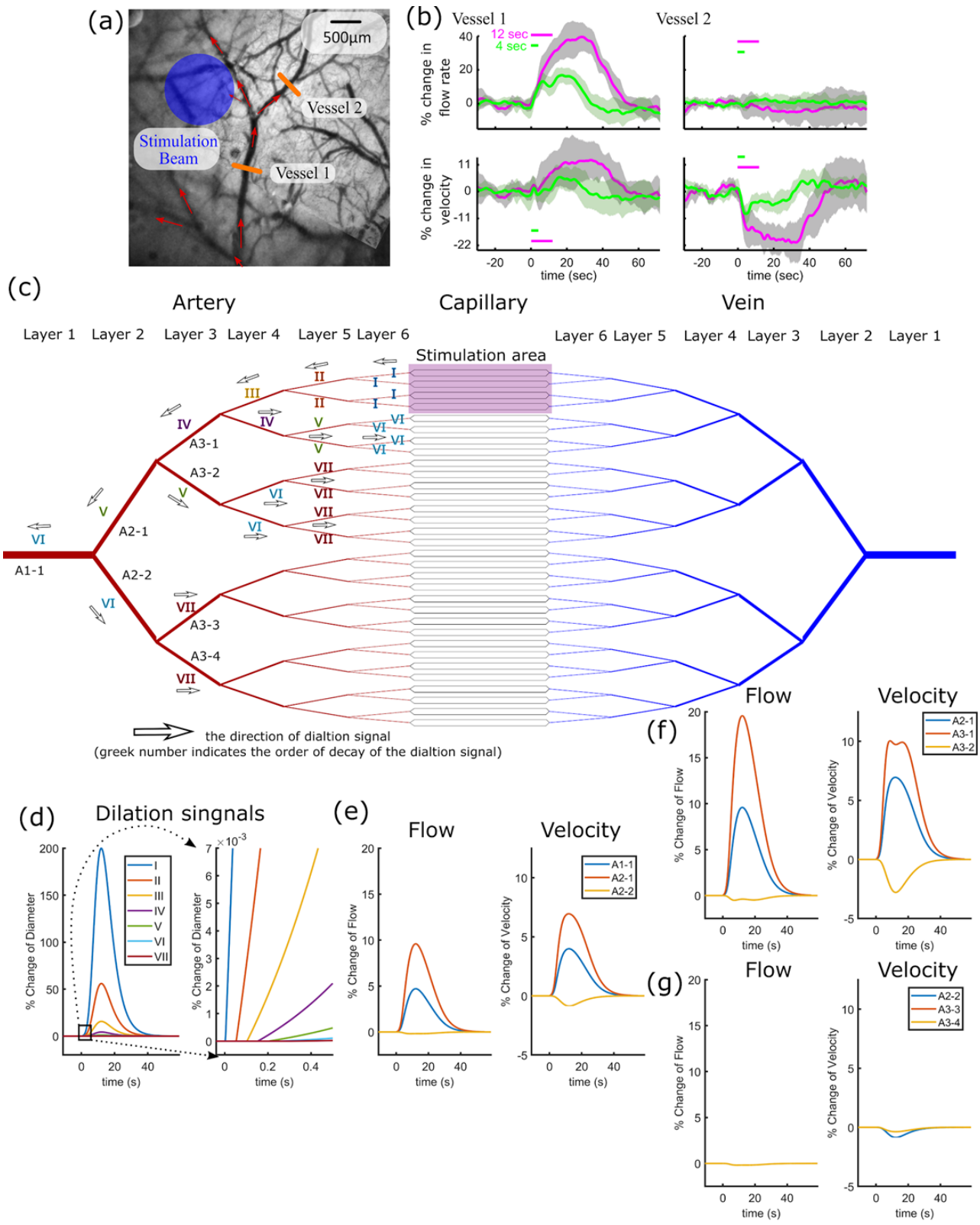


Fig. 19. The possible effect of propagating dilation signal in a microvascular network, (a) an example of a vascular network under study. The red arrows point along the flow direction and the blue circle marks the stimulation area, (b) CBF and velocity responses are shown for $4sec$ and $12sec$ of optical stimulus in vessels 1 and 2. Following the stimulation, blood velocity and CBF both increase in vessel 1. The same stimulation reduces blood velocity in vessel 2 with negligible change in its CBF, (c) to demonstrate the effect of propagating dilation in microvasculature network, we constructed an anatomical model with 13 vascular layers. Blood flows in this network from the artery A1-1 toward the capillary bed in the middle, then out via the vein on the right, (d) the induced dilation propagates along the network but the amplitude of dilation attenuates and the dilation appears with some delay at each layer. Roman numerals indicate the number of vascular branches the dilation signal travels through, (e-g) upstream branches of the stimulation site show an increase in blood flow rate and blood velocity, while adjacent branches typically experience some noticeable drop in the velocity.

velocity in neighboring branches. For instance, a typical case is displayed in Figure 19a. Optogenetic stimulation pulses are delivered in the proximity of one branch of vessel 1. This stimulation leads to dilation of this branch and the increase in the flow and velocity of vessel 1. However, as shown in Figure 19b, blood flow in the other branch has decreased slightly while the drop in the velocity is significant.

This effect is potentially caused by the propagation of dilation signal along vessels through the endothelial cell signaling process. To better investigate this effect, we implemented an anatomical model of cerebral microvasculature which is a model that can emulate the behavior of connected branches. In this model, we had a total of 190 vessel segments, Figure 19c. Each vessel segment is modeled as a resistive fluid component with a diameter that changes for vessels of each layer. This model was adopted from [33] and details, including parameters of fluidic pressure, vessel dimensions and viscosity variables, are available in the reference.

To emulate the acute response, we implemented the propagation of arterial dilation in the cerebrovascular tree [3]. We generated a stimulation-induced vasodilation in a local population of pre-capillary arterioles. The model shows that: 1) this stimulation causes some reduction in the resistance of the targeted arteriole and as a result, blood flow in those vessels and all upstream branches in the same vascular tree increases, 2) the induced dilation propagates to the up- and downstream branches along the vascular tree. This propagated dilation decays over distance. Therefore, the retro-propagated dilation leads to blood flow increases in the nearby arterial branches; however, vessels that are further away from the stimulation site are less affected by this dilation than the nearby vessels. Figure 19d shows the attenuation rate and the delay of dilation signals. Here, Roman numerals indicate the number of branching points that the dilation signal has passed through. This anatomical model also showed that it is reasonable to expect conditions where the blood flow in a parent vessel is increased when one of its daughter branches is experiencing some negligible changes in the flow but noticeable reductions in the velocity. For instance, in this simulation, if we look at the flow and velocity charts for a parent vessel, A1-1, and its branch, A2-2, we can see the dynamics which was observed experimentally before and discussed earlier in this section, Figure 19e. Similar scenarios were also observed in other parts of the network, Figure 19f,g.

I. Effect of the Network Topology on the Vascular Dynamics

The model we developed and tested in this work mainly captures the temporal dynamics of the CBF response. Nonetheless, CBF response is also affected not only by the NVC but also by the topography of vascular network. Obviously, the number and location of branches that bifurcate from a vessel can change the CBF response that we record when we stimulate nearby neurons. One good example is what we usually call the *blood stealing effect*. This happens when the CBF in a branch drops after stimulation because blood flow has shifted its direction toward a parallel-connected branch that has significant reduction in its fluidic resistance. In some experiments, we observed that when we were activating neural population of one area, blood flow and velocity were reducing in neighboring branches which were not directly supplying the activated region. In fMRI data analysis, appearance of a BOLD signal indirectly predicts neural activation while a negative BOLD signal is interpreted as neural deactivation. Our observations prove that such interpretation can be misguiding since blood stealing effect can cause negative BOLD but it should not be interpreted as neural deactivation. In fact, blood stealing effect has been a topic of debate among the fMRI community [39].

In our future steps, we should expand the model to incorporate the effect of the structure of the vascular network. For example, to test this idea we tried to develop a blood flow controller that simultaneously controls CBF in two vessel branches which have coupled dynamics, Figure 20. This experiment allowed us to test the model in complex scenarios where the fluidic resistance of both vessels are precisely controlled via NVC. Some results of this experiment are displayed in Figure 20. This experiment demonstrates the feasibility of developing closed-loop systems which control the flow of blood in large interconnected networks of the brain.

J. Discussion

In this work, optogenetic stimulation was used to modulate cortical activity and we analyzed the spatial-temporal features of evoked LFPs and the consequent vasodynamics in cerebral cortex. The optogenetically induced neural activity was monitored by recording the LFP via transparent surface mounted ECoG electrodes. SD-OCT was used to detect vessel diameter, blood velocity and blood flow changes in selected pial arteries. We developed a biophysical model which was able to reproduce the dynamics of the ChR2+ excitatory and inhibitory neural populations mathematically, and capture the temporal/spectral features of recorded LFP signals.

It was observed in the experiments that optogenetic stimulation triggers changes in blood flow in nearby vessels and this blood flow signal could be decomposed to acute and delayed responses. Currently, there is no mathematical model that can fully describe the acute and delayed responses that are generated by the NVC (see the detailed review by Huneau et al., [34]). The delayed response has been studied in more details compared to the acute response and some models were offered to simulate this process. Majority of these models, known as *balloon models*, are used in the theoretical analysis of fMRI BOLD signals, [35], [36]. Balloon models mathematically describe the metabolic feedback loop of vasoactive substances and the hypothesized effect of the pressure-dependent fluidic capacitance of veins and venules. Nevertheless, recent studies have shown that the effect of fluidic capacitance on the local vascular response is negligible [37] and the metabolic feedback model alone is insufficient to reproduce the temporal characteristics of fMRI BOLD signals [38]. Therefore, there is need for a plausible mathemtical framework to better model blood flow fluctuations that are caused by the NVC.

For this reason, we created several models and we tested the performance of each model in reproducing subtle temporal

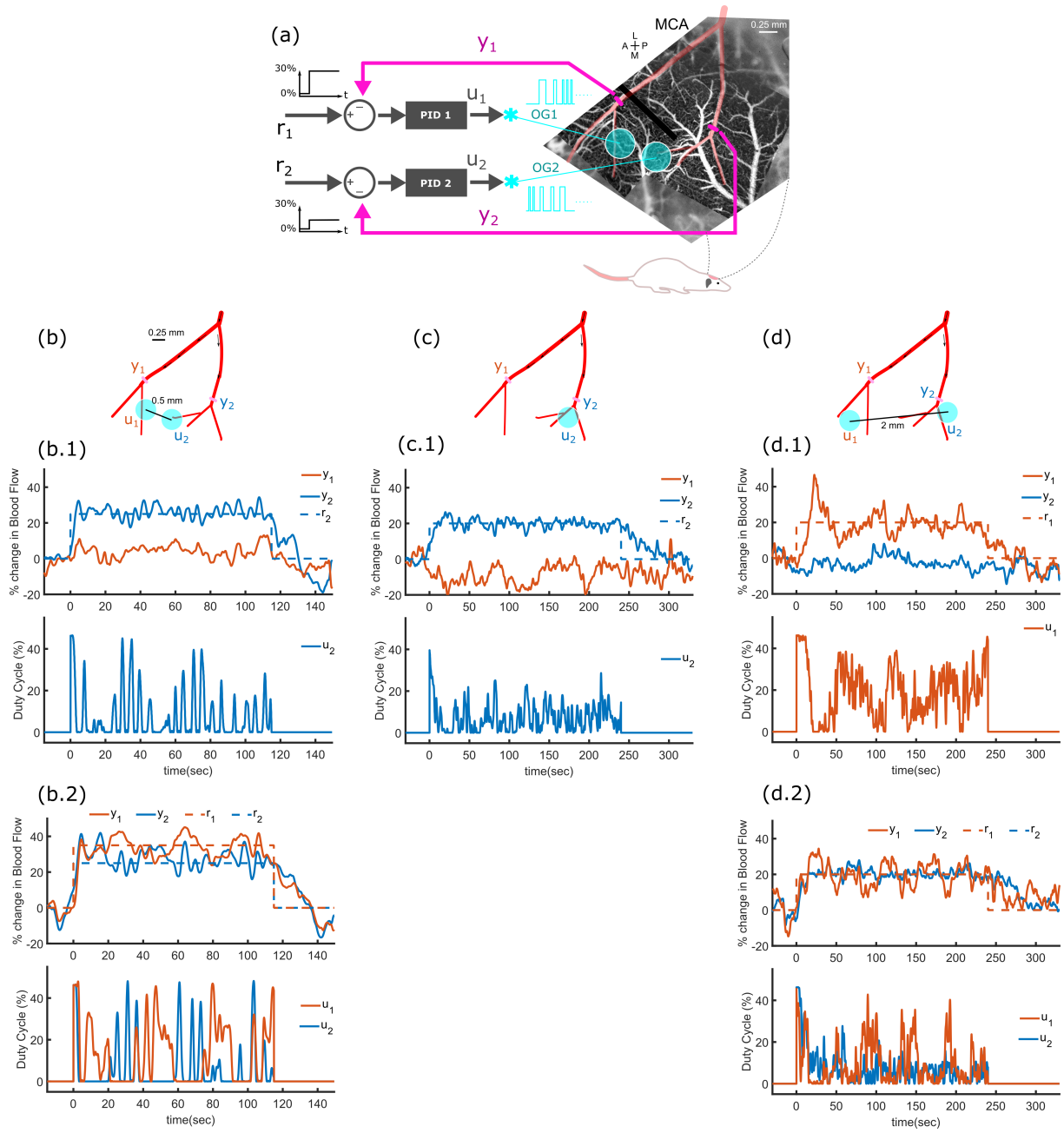


Fig. 20. A pilot study of the interconnectivity of CBF responses: (a) a dual-loop feedback system was designed to control the flow of blood in two vessel branches (y_1 and y_2) simultaneously with separate setpoints r_1 and r_2. Blood flew in y_1 and y_2 were controlled by two independent PID controllers, PID 1 and PID 2, by delivering the stimulation light pulses to two separated neural ensembles, u_1 and u_2, (b) the loci of stimuli for u_1 and u_2 were placed $500\mu m$ apart from each other, (b.1) for vessel y_2, the setpoint was blood flow increase of 25% while the controller of vessel y_1 was off. By delivering light pulses to location u_2 the controller could successfully adjust the CBF response in vessel y_2. However, the light exposure which was delivered to u_2 also evoked some slight CBF response in vessel y_1, possibly due to the relatively short distance between vessel the y_1 and the stimulation area u_2. The location of u_2 was within the feeding territory of vessel y_1, (b.2) in another experiment, the setpoint for vessel y_1 was set to 35% increase while the vessel y_2 setpoint was set to 25% increase in CBF. Despite the interdependent relation between the vessel segment y_1 and the stimulation site u_2, we could adjust the CBF of each branch to the separate predefined levels, (c) the stimulation area for y_2 was moved further away from y_1 by $0.5mm$ to reduce the degree of interdependence between the CBF response in vessel y_1 and the stimulation area u_2, (c.1) CBF response in y_1 and y_2 when the setpoint for the vessel y_2 was 20% while the controller of vessel y_1 was off. Delivering light to u_2 did not increase the CBF in vessel y_1 but caused some reduction in the flow of vessel y_1, (d) the distance between stimulation sites were increased to $2mm$, (d.1) the setpoint for vessel y_1 was set to 20%, while the controller of vessel y_2 was off. Results indicated that stimulation at u_1 had insignificant effect on the CBF of vessel y_2 while the CBF in vessel y_1 was adjusted to the desired setpoint.

features of the CBF response. Our studies showed that both acute and delayed responses undershoot after an initial rapid increase in the blood flow. This dynamics resembles the behavior of a damped oscillator. Therefore, as we expected, after studying different models, we realized that the only model that could recreate main features of the CBF response should have two parallel pathways in its structure where each pathway mathematically emulates the function of a damped oscillator.

Generally, NVC models can predict CBF response accurately in the range of tens of seconds, but fail for larger timescales [34]. Our analysis of the closed-loop blood flow controller data confirmed that the proposed model, once trained by the initial portion of the data, can accurately predict the CBF response for the rest of the period and its accuracy remained acceptable even when the model was used to predict the blood flow dynamics which was recorded for different setpoints without further training of the model. Therefore, in addition to recreating some fine (in the range of seconds) temporal dynamics, the model predictions remained valid up to several minutes. This observation implies that the model is able to capture salient characteristics of the coupling between the vascular and neural activity. Moreover, these results also imply that the relationship between light stimulation and the CBF response remains unplastic and only alters minimally even for larger time-scales.

Since the traditional approach of inducing neural activity (i.e. sensory stimulation) lacks spatial specificity, it is challenging to use this stimulation paradigm to study spatial relations between neural activity and the vascular response. In comparison, optical neuro-stimulation offers great cell-type and spatial specificity and was employed in the current study to investigate such spatial dependencies. We investigated responses of different vessel branches when delivering stimulation pulses to various locations on the cortical tissue and demonstrated that the developed model can capture important temporal features of the blood flow dynamics. For this purpose, only one set of temporal parameters was used and the spatial dependencies were accounted for via tuning the efficacy parameters (ϵ_A and ϵ_D). We concluded that the primary temporal features of the CBF response are consistent under different spatial configuration of stimulation inputs. Furthermore, we observed that delayed response in vessel branches are stronger in amplitude compared to the acute response. However, the acute response of the same vessel can be evoked by stimulating more distal neural populations compared to the delayed response. Similarly, Hillman and colleagues reported that the CBF response of branches close to an activated neural population possesses acute and delayed components whereas the response of distal parallel-connected branches only shows the acute component [3]. One hypothesis is that since the acute response is conducted by the signaling mechanism of endothelium cells, its effect can propagate farther compared to the molecular diffusive mechanism which conducts the delayed response.

Here, we developed our model to identified healthy animals temporal parameters as well as the size and topography of the sensitivity maps for both acute and delayed responses. Similar analysis can be applied to subjects with pathological conditions such as Alzheimer's disease to determine the difference in the CBF responses at different stages of the disease. This approach can lead to the invention of new diagnostic procedures.

ACKNOWLEDGEMENT

This project was supported by the Army Research Office (ARO) grant number: W911NF1810323, the National Science Foundation (NSF) Career Award grant number: 1454300, the National Science Foundation (NSF) grant number: CBET-1830145, and the University of Wisconsin-Milwaukee Research Growth Initiative (RGI) grant number: 101X378.

REFERENCES

[1] Hillman, E. M. C. "Coupling Mechanism and Significance of the BOLD Signal: A Status Report," Annu. Rev. Neurosci. 37, (2014).
[2] Iadecola, C. "The Neurovascular Unit Coming of Age: A Journey through Neurovascular Coupling in Health and Disease," Neuron 96, 1742 (2017).
[3] Chen, B. R., Kozberg, M. G., Bouchard, M. B., Shaik, M. A. and Hillman, E. M. C. "A critical role for the vascular endothelium in functional neurovascular coupling in the brain," J. Am. Heart Assoc. 3, (2014).
[4] Longden, T. A. et al. "Capillary K+-sensing initiates retrograde hyperpolarization to increase local cerebral blood flow," Nat. Neurosci. 20, (2017).
[5] Cai, C. et al. "Stimulation-induced increases in cerebral blood flow and local capillary vasoconstriction depend on conducted vascular responses," Proc. Natl. Acad. Sci. 115, (2018).
[6] R. Pashaie et al., "Optogenetic Brain Interfaces," IEEE Reviews on Biomedical Engineering, vol. 7, pp. 3-30, 2014.
[7] F. Zhang et al., "Circuit-breakers: optical technologies for probing neural signals and systems," Nat Rev Neurosci., vol. 8, pp. 577-581, 2007.
[8] F. Zhang et al., "Multimodal fast optical interrogation of neural circuitry," Nature, vol. 446, pp. 633-639, 2007.
[9] E. S. Boyden et al., "Millisecond-timescale, genetically targeted optical control of neural activity," Nature Neuroscience, vol. 8, pp. 1263-1268, 2005.
[10] K. Deisseroth, "Optogenetics," Nature Methods, vol. 8, no. 1, pp. 26-29, 2011.
[11] Farid Atry, Rex Chen, J. Pisaniello, S. Brodnik, A. Suminski, J. Novello, J. Ness, J. Willimas and Ramin Pashaie, "Optogenetic interrogation and manipulation of vascular blood flow in cortex," Journal of Neural Engineering, Vol. 15, 056033, 2018.
[12] Farid Atry, Seth Frye, Thomas J. Richner, Sarah K. Brodnick, Alana Soehartono, Justin Williams, Ramin Pashaie, "Monitoring Cerebral Hemodynamics Following Optogenetic Stimulation via Optical Coherence Tomography," IEEE Transaction on Biomedical Engineering, vol. 62, no. 2, pp. 766-773, 2015.
[13] Farid Atry, Israel De La Rosa, Kevin Rarick, Ramin Pashaie, "Design and implementation guidelines for a modular spectral-domain optical coherence tomography scanner," International Journal of Optics, Vol. 2018, Article ID 3726207, 22pages.
[14] Farid Atry, Ramin Pashaie, "Analysis of Intermediary Scan-Lens and Tube-lens Mechanisms for Optical Coherence Tomography," Applied Optics, Vol. 5, No. 4, pp. 646-653, 2016.
[15] Dong-Wook Park, Sarah Brodnick, Jared Ness, Farid Atry, Lisa Krugner-Higby, Amelia Sandberg, Solomon Mikael, Thomas Richner, Joseph Novello, Hyungsoo Kim, Dong-Hyun Baek, Jihye Bong, Cuong Nguyen, Seth Frye, Sanitta Thongpang, Kyle Swanson, Wendell Lake, Ramin Pashaie, Justin Williams, and Zhenqiang Ma, "Fabrication and utility of a transparent graphene neural electrode array for electrophysiology, in vivo imaging, and optogenetics," Nature Protocols, doi:10.1038/nprot.2016.127, Oct. 2016.
[16] Amelia A. Schendel, Dong-Wook Park, Solomon Mikael, Thomas J. Richner, Sarah K. Brodnick, Farid Atry, Seth Frye, Ramin Pashaie, Sanitta Thongpang, Justin C. Williams and Zhenqiang Ma, "Carbon Layered Electrode Array (CLEAR) technology for neural imaging and optogenetic applications," Nature Communications, vol. 5, no. 5258, pp. 1-11, 2014.

[17] Thomas J Richner, Sanitta Thongpang, Sarah K Brodnick, Amelia A Schendel, Ryan W Falk, Lisa A Krugner-Higby, Ramin Pashaie, and Justin C Williams, "Optogenetic micro-electrocorticography for modulating and localizing cerebral cortex activity," Journal of Neural Engineering, 11, 016010 (12pp), Jan. 2014.
[18] Mehdi Azimipour, Ryan Baumgartner, Yuming Liu, Steven Jacques, Kevin Eliceiri, Ramin Pashaie, "Extraction of Optical Properties and Prediction of Light Distribution in Rat Brain Tissue," Journal of Biomedical Optics, Vol. 19, No. 7, 075001, July, 2014.
[19] Mehdi Azimipour, Farid Atry, Ramin Pashaie, "Effect of Blood Vessels on Light Distribution in Optogenetic Stimulation of Cortex," Vol. 40, Issue 10, pp-2173-2176, Optics Letters, 2015.
[20] Nikolic, K. et al. "Photocycles of channelrhodopsin-2," Photochem. Photobiol. 85, 400411 (2009).
[21] Devor, A. et al. Suppressed neuronal activity and concurrent arteriolar vasoconstriction may explain negative blood oxygenation level-dependent signal. J. Neurosci. 27, 44529 (2007).
[22] Friston, K. J., Harrison, L. and Penny, W. "Dynamic causal modelling," Neuroimage 19, 1273302 (2003).
[23] Marreiros, A. C., Kiebel, S. J. and Friston, K. J. "Dynamic causal modelling for fMRI: A two-state model," Neuroimage 39, 269278 (2008).
[24] Havlicek, M. et al. "Physiologically informed dynamic causal modeling of fMRI data," Neuroimage 122, 355372 (2015).
[25] Buzsaki, G., Anastassiou, C. A. and Koch, C. The origin of extracellular fields and currents-EEG, ECoG, LFP and spikes. Nat. Rev. Neurosci. 13, 407420 (2012).
[26] Williams, J. C. et al. "Computational Optogenetics: Empirically-Derived Voltage- and Light-Sensitive Channelrhodopsin-2 Model," PLoS Comput. Biol. 9, 1719 (2013).
[27] Friston, K. J., Mechelli, A., Turner, R. and Price, C. J. "Nonlinear Responses in fMRI: The Balloon Model," Volterra Kernels, and Other Hemodynamics. Neuroimage 12, 466477 (2000).
[28] Friston, K. J. et al. "Dynamic causal modelling revisited," Neuroimage 01 (2017). doi:10.1016/j.neuroimage.2017.02.045
[29] David, O. et al. Identifying Neural Drivers with Functional MRI: An Electrophysiological Validation. PLoS Biol. 6, e315 (2008).
[30] Szkulmowski, M., Szkulmowska, A., Bajraszewski, T., Kowalczyk, A. and Wojtkowski, M. "Flow velocity estimation using joint Spectral and Time domain Optical Coherence Tomography," Opt. Express 16, 6008 (2008).
[31] Destexhe, A., Mainen, Z. F. and Sejnowski, T. J. "Synthesis of models for excitable membranes, synaptic transmission and neuromodulation using a common kinetic formalism," J. Comput. Neurosci. 1, 195230 (1994).
[32] McCormick, D. A., Wang, Z. and Huguenard, J. "Neurotransmitter Control of Neocortical Neuronal Activity and Excitability," Cereb. Cortex 3, 387398 (1993).
[33] Boas, D. A., Jones, S. R., Devor, A., Huppert, T. J. and Dale, A. M, "A vascular anatomical network model of the spatio-temporal response to brain activation," Neuroimage, Vol. 40, pp. 11161129, 2008.
[34] Huneau, C., Benali, H. and Chabriat, H., "Investigating human neurovascular coupling using functional neuroimaging: A critical review of dynamic models," Front. Neurosci. Vol. 9, 2015.
[35] Buxton, R. B., Wong, E. C. and Frank, L. R., "Dynamics of blood flow and oxygenation changes during brain activation: The balloon model," Magn. Reson. Med., Vol. 39, pp. 855864, 1998.
[36] Mandeville, B., Marota, J. J. A., Moskowitz, M. A., Rosen, R. and Weisskoff, M., "Evidence of a Cerebrovascular Postarteriole Windkessel With Delayed Compliance," pp. 679689, 1999.
[37] Lorthois, S., Cassot, F. and Lauwers, F., "Simulation study of brain blood flow regulation by intra-cortical arterioles in an anatomically accurate large human vascular network. Part II: Flow variations induced by global or localized modifications of arteriolar diameters," Neuroimage, Vol. 54, pp. 28402853, 2011.
[38] Lundengard, K. et al., "Mechanistic Mathematical Modeling Tests Hypotheses of the Neurovascular Coupling in fMRI," PLoS Comput. Biol., Vol. 12,pp. 128, 2016.
[39] D. Bressler, N. Spotswood, and D. Whitney, Negative BOLD fMRI Response in the Visual Cortex Carries Precise Stimulus-Specific Information, PLoS One, vol. 2, no. 5, p. e410, May 2007.
[40] K. Nikolic, N. Grossman, M. S. Grubb, J. Burrone, C. Toumazou, and P. Degenaar, Photocycles of channelrhodopsin-2, Photochem. Photobiol., vol. 85, no. 1, pp. 400411, 2009.